TOHOKU
UNIVERSITY

博 士 学 位 論 文
Doctoral Thesis

論文題目　　　Evaluation of New Chelator for the Development of Diagnostic and Therapeutic Radiopharmaceuticals: DFT Calculation, and *In Vitro* Evaluation

提 出 者　　　東北大学大学院医工学研究科

　　　　　　　医工学専攻

　　　　　　　学籍番号/ID NO　COWD 1006

　　　　　　　氏　　　名/Name　DANNI RAMDHANI

指 導 教 員	渡部 浩司		教授
審 査 委 員 （○印は主査）	○ Hiroshi Watabe 1 Takaaki Abe 3 Shozo Furumoto 5		2 Kazutaka Murayama 4 6

提　出　者　略　歴			
ふり 　　　 ,氏 がな 　　　 ,名	DANNI RAMDHANI		昭　和 西　暦
本　籍		都・道 府・県	国　籍
履　歴　事　項			
【 学　歴 】			

【 職　歴 】	

備考１）外国人留学生は、国籍を記入してください。
　　　２）履歴事項は、大学入学から年次にしたがって記入してください。

TOHOKU UNIVERSITY
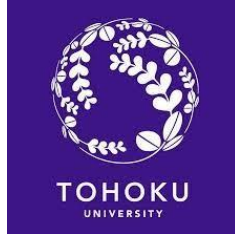
DOCTORAL THESIS

Evaluation of New Chelator for the Development of Diagnostic and Therapeutic Radiopharmaceuticals: DFT Calculation, and *In Vitro* Evaluation

Author:
Danni RAMDHANI

Supervisor:
Prof. Hiroshi WATABE

A Dissertation Submitted in Fulfillment of the Requirements for the Award of the Degree of Doctor of Philosophy in Biomedical Engineering
in the

Department of Biomedical Engineering

Graduate School of Biomedical Engineering

Tohoku University

January 24th, 2024

TOHOKU UNIVERSITY

Abstract

Doctor of Philosophy

Evaluation of New Chelator for the Development of Diagnostic and Therapeutic Radiopharmaceuticals: DFT Calculation, and *In Vitro* Evaluation

by Danni RAMDHANI

The 1,4,7,10-tetrazacyclodecane-1,4,7,10-tetracetic acid (DOTA) as an important chelator in a series of precursor DOTA-TATE (DOTA-[Tyr3]-Octreotate) approved by the FDA for the diagnosis (^{68}Ga-DOTA-TATE) and treatment (^{177}Lu-DOTA-TATE) of somatostatin receptor positive neuroendocrine tumors (NETs). DOTA has been widely used as a stable chelator of tri positive radiometals such as ^{68}Ga^{3+}, ^{111}In^{3+}, ^{177}Lu^{3+}, $^{86/90}$Y^{3+}, $^{44/47}$Sc^{3+}, ^{213}Bi^{3+}, and ^{225}Ac^{3+}, although labeling must be done at high temperatures (80–95°C) to get a high radiochemical conversion (RCC). In this study, we evaluate the 4-[2-(bis-carboxy-methylamino)-5-(4-nitrophenyl)-entyl])-7-carboxymethyl-[1,4,7]tri-azonan-1-yl acetic acid (3p-*C*-NETA) chelator using DOTA as a benchmark. As an initial evaluation, we perform density functional theory (DFT) calculations to compare the formation constant of the formed chelator-radiometal complex. We made a comparison of several chelators (DOTA, 3p-*C*-NETA, and 3p-*C*-DEPA), to radiometals Lu^{3+}, Bi^{3+}, and Ac^{3+}. Then, we performed an *in vitro* evaluation of 3p-*C*-NETA-TATE compared to DOTA-TATE labeled with Lu^{3+}.

DFT calculation performed with M06-HF/6-311G(d) as the functional/basis sets by applying the continuum solvation model of solvation model density (SMD) and conductor-like screening model (COSMO). Radionuclide ^{177}Lu was used to label 3p-*C*-NETA-TATE and DOTA-TATE with various concentrations (0.1-20 μM), at temperatures (40-95°C). The *in vitro* stability of the corresponding radiocomplexes was determined in phosphate-buffered saline (PBS) and human serum (HS). Cell binding and internalization studies were conducted on somatostatin receptor 2 (SSTR2) expressing human NET cell lines, BON-1 (pancreatic NET) (BON-1-SSTR2) at time intervals of 5 min - 3 days. The cell viability test was carried out using the MTT assay on 22 series of activities: 3KBq – 150 MBq. Clonogenic assay with glutaraldehyde (6.0% v/v), stained with crystal violet (0.5% w/v) with variation 0.1; 0.6; 1.3; 1.7MBq/well. The biodistribution test was carried out by labeling 3p-*C*-NETA-TATE using the Al^{18}F method, where the addition of

gelofusine aims to obtain information on reducing the renal retention of radiolabeled peptides. The 3p-*C*-NETA chelator's formation constant computation reveals that Ac^{3+} has a lower stability of complex formation than Lu^{3+} or Bi^3. In contrast, 3p-*C*-DEPA has a better formation constant for Ac^{3+}, and Bi^{3+} which has a large ionic atomic radius, slightly lower results compared to Lu^{3+}. Radiolabelling showed that [^{177}Lu]Lu-3p-*C*-NETA-TATE at a concentration of 10μM, 40°C showed better RCC than [^{177}Lu]Lu-DOTA-TATE. For the stability test, both complexes showed good stability in PBS and HS for up to 3 days, and decreased % intact radiocomplex on days 5 and 7. Cell binding and internalization studies showed the same profile where internalization into cells began to occur at 120 minutes, as well as blocking studies showed no internalization of the two compounds into cells. DFT calculation, and pre-clinical evaluation show [^{177}Lu]Lu-3p-*C*-NETA-TATE is promising for use in therapy and diagnostics (theranostic) of NETs.

Acknowledgments

Contents

List of Figures

List of Tables

List of Abbreviations

DOTA	1,4,7,10-tetrazacyclodecane-1,4,7,10-tetracetic acid
DOTA-TATE	(DOTA-[Tyr3]-Octreotate)
3p-*C*-NETA	4-[2-(bis-carboxy-methylamino)-5-(4-nitrophenyl)-entyl])-7-carboxymethyl-[1,4,7]tri-azonan-1-yl acetic acid
RPs	Radiopharmaceuticals
NETs	Neuroendocrine Tumors
DFT	Density Functional Theory
SMD	Solvation Model Density
COSMO	Conductor-like Screening Model
PBS	Phosphate-Buffered Saline
SSTR2	Somatostatin Receptor Type 2
BON-1-SSTR2	Somatostatin Receptor 2 (SSTR2) expressing human NET cell lines, BON-1 (pancreatic NET)
Theranostic	Therapy and Diagnostics
PET	Positron-Emission Tomography
SPECT	Single Photon Emission Computed Tomography
BFCs	Bifunctional Chelates
TRT	Targeted Radionuclide Therapy
mAb	monoclonal antibodies
LET	Linear Energy Transfer
MTT	3-(4,5-dimethylthiazol-2-yl)-2-5-diphenyltetrazolium bromide
AEs	Auger Electrons
TAT	Targeted Alpha Therapy
DSBs	Double Strand Breaks

Chapter 1

Introduction

1.1 Background

The application of radioisotopes in radiopharmaceuticals has been growing rapidly as a radiotracer for cancer imaging via Positron-Emission Tomography (PET) or Single-Photon Emission Computed Tomography (SPECT), and also for therapeutic purposes by utilizing α, β-particles, or auger electron emission. This introduction briefly describes the imaging and therapeutics used in radiopharmaceuticals, followed by the role of bifunctional chelates (BFCs) as an important component in the successful use of radiopharmaceutical compounds. The BFCs in general called chelator or ligand functions to bind radiometal strongly and form complex radiometal compounds with high thermodynamic stability and fast radiolabeling kinetics under mild conditions.

Methods for designing radiometal and BFC based compounds have been outlined here, to provide an overview of how radiopharmaceutical compounds are assessed for use *in vivo*. Radioisotopes commonly used for imaging are ^{99m}Tc, ^{18}F, ^{68}Ga, ^{64}Cu, ^{86}Y, 1^{11}In, and ^{89}Zr, and for therapeutic purposes are ^{131}I, ^{90}Y, ^{177}Lu, ^{161}Tb, ^{225}Ac, ^{213}Bi ^{211}At, ^{212}Pb, and $^{186/188}$Re. Overview of the decay of radionuclides and their features are described in table 1.1.

The stability of the radiometal-ligand complex is determined by the electrostatic interactions and steric constraints, which are caused by the structural chemical properties of the radiometal ion such as ionic radius, geometric coordination. Almost all radiometals are employed with some of these well-established ligands that are used in clinical and research settings, although there are fundamental differences in the structural chemistry of the radiometal, this is what has limited its use. The DOTA chelator is currently the gold standard, in wide use for radionuclides tri positive radiometals such as ^{68}Ga^{3+}, ^{111}In^{3+}, ^{177}Lu^{3+}, $^{86/90}$Y^{3+}, and $^{44/47}$Sc^{3+} [1].

Table 1.1. Overview of the decay of radionuclides and their features

Type of Particles	Objectives for cancer	Penetration in tissue (mm)	Wave composition	Radioisotopes
Gamma (γ)	Imaging	stopped by 50 mm of lead.	Electromagnetic wave ($_0^0\gamma$)	^{131}I, ^{123}I, ^{111}In, ^{99m}Tc and ^{67}Ga
Positron (β$^+$)	Imaging	0.6	Electron ($_{+1}^0e$))	^{89}Zr, ^{68}Ga, ^{18}F, ^{124}I, and ^{64}Cu
Auger Electrons (AEs)	Therapy	< 0.0005	Electron ($_{-1}^0e$)	^{201}TI, ^{161}Tb, ^{11}1In, ^{99m}Tc, ^{67}Ga, and ^{64}Cu
Beta$^-$ (β$^-$)	Therapy	0.5 to 12	Electron ($_{-1}^0e$)	^{177}Lu, ^{161}Tb, ^{131}I, and ^{90}Y
Alpha (α)	Therapy	0.02 to 0.1	2 proton, 2 neutron ($_2^4$He)	^{227}Th, ^{225}Ac, ^{224}Ra, ^{223}Ra, ^{213}Bi, ^{212}Pb, ^{211}At, and ^{149}Tb

1.2 Radiopharmaceutical Chemistry

In nuclear medicine, radiopharmaceutical chemistry plays an essential part in developing novel imaging techniques and targeted therapies to solve important health issues, especially cancer. Globally, in 2023 it is estimated that there will be 20 million new cases of cancer and 10 million deaths by cancer. Early detection and patient management can decrease the burden of cancer, and in this respect, nuclear imaging and therapies have significantly improved clinical medicine. The use of radioisotopes in diagnostic and therapies techniques in medicine is important.

Radioisotopes can be used in conjunction with imaging tools that record the gamma rays emitted from within to image the dynamic processes occurring in various bodily areas. A radioactive dosage is administered to the patient when utilizing radiopharmaceuticals (RPs) for diagnosis, and the amount of activity in the organ can then be analyzed as either a two-dimensional visualization or, with the use of tomography, as a three-dimensional image. Gamma rays are emitted from within the body by radiopharmaceutical compounds that use radioactive tracers. These tracers are typically short-lived isotopes linked to chemical compounds that enable the study of certain physiological processes.

1.2.1. Radiopharmaceutical for Imaging

Clinical medicine now routinely uses non-invasive techniques to visualize tumors and track their growth, all of which have proven crucial to patient survival. The SPECT and PET are two imaging modalities that are heavily utilized in nuclear medicine. In both techniques, the radionuclides must be injected into the patient; the radioactivity is

connected to a targeting moiety that sends the radionuclides to the tumor site. Cameras use the photons or particles emitted to detect them, and the result is a 3D image showing the body's radioactivity accumulation in relation to the tumor's location. The clinical application of SPECT and PET is determined by a variety of variables, including cost, the resolution and sensitivity of the imaging method, and the accessibility of a suitable radioisotope [2].

1.2.1.1. Single-Photon Emission Computed Tomography (SPECT)

The primary function of nuclear medicine imaging technology is to detect gamma-ray photons from radioisotopes that decay in the tissue of the patient being scanned. The gamma-emitting radionuclide ^{99m}Tc was discovered in 1937, and in 1960 the ^{99}Mo/^{99m}Tc generator system was employed for the first time, starting in a period of widespread application for compounds labeled with ^{99m}Tc in clinical SPECT imaging. Currently, 70–80% of all radio-diagnostic scans still employ it for medical imaging.

Gamma cameras/detectors are specifically designed for energy windows of 100-250 keV, and γ-rays outside this energy range will result in poor image quality. Therefore, in order for SPECT radionuclides to be diagnostically useful, their decay energy must be within this range. The current development of the SPECT system not only detects radiotracer in the body with concentrations of 10^{-6} and 10^{-9} M, but has now been able to show sensitivity up to nanomolar and even picomolar [3, 4]. The most used radionuclides for diagnostic purposes in SPECT nuclear medicine are listed in Table 2.

Table 1.2. Radionuclides for imaging applications in SPECT Nuclear Medicine applications

Radioisotope	Decay Mode	Energy Emission	Half-Life (Hour/Day)
^{99m}Tc	Isomeric transition	140 keV	6.03 h
^{201}Tl	Electron capture	68-80 keV	3.05 d
^{67}Ga	Electron capture	93- 300 keV	3.26 d
^{111}In	Electron capture	171-245 keV	2.8 d
^{123}I	Electron capture	159 keV	13.2 h
^{133}Xe	Beta emission	81 keV	5.25 d

1.2.1.2. Positron-Emission Tomography (PET)

PET scans create finely detailed, three-dimensional images of the inside of the body. The images can clearly display the body portion under investigation, along with any abnormal areas, and they can draw attention to how well-functioning specific bodily processes are. PET is a type of nuclear medicine procedure that measures the metabolic activity of the cells of body tissues.

A radionuclide that emits a positron as a result of β^+ decay is needed for PET. The positron loses energy as a result of interactions with tissue, and after moving a short distance (usually approximately 1 mm), it will split into two gamma-ray photons with energies of 511 keV each. As a result, these photons will track in equal and opposing directions if the photons don't have any further interactions. However, Compton scattering may occur to some extent for each photon (or both), causing a tiny modification to the 180-degree. Additionally, the positron may have residual momentum before it decays, which is reflected in the net momentum of the emitted gamma-ray photons. The angle difference between photons will, however, often be less than 0.25 degrees [5].

In 1975, the first PET for industrial use was developed, the short half-life isotopes ^{18}F, ^{15}O, ^{13}N, and ^{11}C, whose manufacture depended on an on-site cyclotron, were the primary supply of PET imaging agents for several decades. Today, ^{18}F (t1/2 = 109 min) is the radioisotope most commonly used for PET imaging. This radioisotope is easily accessible daily from commercial sources, reducing the requirement for an on-site cyclotron. Though a lot of research has been put into creating β^+ emitting radioisotopes of metals like Ga, Y, Zr, and Cu that have different half-lives and can get around some of the synthetic restrictions still connected with incorporating organic + emitting nuclides into small drug mimics, the field is still in its infancy [6, 7].

PET has higher sensitivity (up to 10^{-12} M, compared to 10^{-6} M for SPECT) and higher resolutions (2 - 4 mm or lower compared to 6 – 8 mm for SPECT) than its single-photon analogue. PET has a relationship with the inherent characteristics of β^+ emission for both resolution and sensitivity. First, the resolution is influenced by the initial distance that the β^+ travels before annihilation, which is influenced by the energy of decay. In order to provide higher resolution images, lower energy β^+ emission is preferred in PET.

Secondly, The coincident detection of two -rays also contributes to the great sensitivity. In spite of the benefits of PET imaging, SPECT is more frequently employed in clinical settings, probably simply because it is a more well-established technology [7, 8]. The radionuclides utilized in PET/CT studies are listed in table 3.

Table 1.3. Summary of radionuclides used in PET/CT studies

Isotope	Half-life (minutes)	Production mode
^{18}F	110	Cyclotron
^{11}C	20	Cyclotron
^{13}N	10	Cyclotron
^{15}O	2	Cyclotron
^{68}Ga	68.3	Generator
^{82}Rb	1.27	Generator

1.2.2. Radiopharmaceutical for Therapy

A potent cancer treatment method known as targeted radionuclide therapy (TRT) uses high-affinity tumor-targeting vehicles, such as monoclonal antibodies (mAb), peptides, or small molecules, for selectively delivering doses of ionizing radiation from radionuclides to target cancer cells, while minimizing radiation exposure to surrounding healthy cells. Ionization has to terminate in irreparable DNA double-strand helix damage in order to kill the cell. For radiotherapy, emitters of beta particles (β^-), alpha particles (α), and Auger electrons can be utilized [9].

The initial benefit of TRT is that tumors, including metastatic sites, can be targeted with it. Precise therapeutic dose delivery can be obtained by first using RPs for imaging purposes in determining the uptake of RPs in target tissues. Second, an extensive variety of radionuclides with various radiation types and intensities are now readily accessible. For instance, killing resistant hypoxia cells with high linear energy transfer (LET) radionuclides is functioning properly. Thirdly, this treatment provides a significantly smaller whole-body absorbed dose. TRT can be an adjunctive therapy, along with or after other treatments such as chemotherapy and surgery. When conventional therapy or chemotherapy is ineffective for systemic metastatic cancer, it is utilized to reduce symptoms, shrink, and stabilize tumors [10-12].

The physical properties of radionuclides must be considered carefully when selecting them for therapeutic use. These include radionuclide purity, physical half-life, radiation energy, emissions type, daughter products, in vivo stability, toxicity, the delivery strategy, and how their chemistry interacts with the carrier molecule. Concerning the carrier, Its specificity and stability must be confirmed: transport of a chemical molecule through a cell membrane, receptor binding sites, transportation of cell damaged from circulatory system, physical particles entrapment, metabolic cycling, and clearance rate. The condition will have an impact on the radionuclide concentration ratio between the tumor and surrounding normal tissues. The condition will have an impact on the ratio of radionuclide levels in the tumor to that in healthy tissues. This ratio needs to be improved. Longer radiation exposure will be given to the target tumor and its surroundings by RPs with lengthy half-lives. However, due to the delivery duration, RPs with a relatively short physical half-life have restrictions [13, 14].

The main radionuclides utilized in TRT are Auger electrons (AEs) (4-26 keV/m), beta (β)-particles (0.2 keV/m), or alpha (α)-particles (50-230 keV/m) emitters. Ionizing particles are emitted by each of these radiations as they travel and are then deposited in the specific target cells. The radiation both directly and indirectly damages the cell [10].

1.2.2.1. Auger electrons (AEs)

Radionuclides that decay via electron capture, such as ^{111}In, ^{67}Ga, ^{99m}Tc, ^{195m}Pt, ^{125}I, and ^{123}I, produce very low-energy electrons known as auger electrons (AEs). The high LET that results from the deposition of this energy over nanometer-micrometer distances has the potential to kill cancer cells, specifically if they are released close to cell-sensitive targets like DNA and the cell membrane. As a result, radiotherapeutic agents that emit AE have a lot of potential for treating cancer [15, 16].

Table 1.4. Features radionuclides emitting Auger electrons

| Radionuclide | Auger electrons (AEs) | | | | Internal conversion (IC) electrons | | |
	Half-life	AEs/ decay	Average AE energy per decay (keV)	Average energy per AE (keV)	IC electrons/ decay	Average IC electron energy released per decay (keV)	Average energy per IC electron (keV)
^{125}I	57 d	23.0	12.0	0.5	0.9	7.3	7.7
^{123}I	13 h	13.7	7.2	0.5	02	21.0	222.6
^{67}Ga	78 h	5.0	6.6	1.3	0.3	29.7	14.1
^{99m}Tc	6 h	4.4	0.9	0.2	1.1	15.2	13.8
^{111}In	67 h	7.4	6.9	0.9	0.2	27.9	176.1
^{201}Tl	73 h	20.9	14.8	0.7	0.9	29.9	32.9
^{191}Pt	2.8 d	14	17.8	1.3	304	57.1	0.2
^{193m}Pt	4.3 d	27.4	10.9	0.4	3.0	126.8	42.4
^{195m}Pt	4.0 d	36.6	23.1	0.6	2.8	161.4	58.1
^{197}Hg	64.1 h	23.2	16.1	0.7	0.8	54.1	67.0
^{197m}Hg	23.8 h	19.4	13.5	0.7	1.6	203.5	127.0
^{119}Sb	38.2 h	23.7	8.9	0.4	0.8	17.0	20.2
^{161}Tb[b]	6.9 d	0.9[c]	5.1[c]	5.7	1.4	36.7	26.2

[a]The MIRD Radionuclide and Decay Schemes were used to calculate the number of AEs and IC electrons (Eckerman and Endo 2008).
[b]The National Nuclear Data Center provided the number of AEs and IC electrons for 161Tb (65-Terbium-161 2011).
[c]Calculation based only on Auger electrons in the K and L shells

1.2.2.2. Beta-Particles (β⁻)

Over the past 40 years, beta particles have been employed in the treatment of cancer. They are produced as a result of the process of decay, in which an unstable nucleus is changed into a proton and a high-energy electron. Particles have a negative charge. Some of them, including ^{32}P, ^{89}Sr, ^{90}Y, and ^{169}Er, produce gamma (γ) rays and have a considerably long path from 0.0 to 12 mm. They emit rays at a 10% level that is appropriate for imaging to verify tumor uptake, biodistribution, and dosimetric calculations. Compared to alpha particles, they have a low LET of about 0.2 keV/m, hence more beta particles are needed to produce the same absorbed dosage [17, 18].

1.2.2.3 Alpha-Particles (α)

In 2013, the application of targeted particle treatment (TAT) was approved. Due to their high energy and short travel lengths, alpha particles are more effective in specific applications. For various micrometastases, TAT is an appealing treatment approach. Multiple lesions may be treated at once, and it is simple to give. In order to treat cancer, it is also feasible to combine it with other therapeutic modalities. A ^{4}He nucleus (sometimes abbreviated as (He^{2+}) is an alpha particle if it is absent of the electrons that

surround it. When a radioactive atom undergoes decay, its nucleus emits alpha radiation with an energy of 4 to 9 MeV. These particles travel only a few cell diameters (40 to 100 m) through tissue. The particles have high LET (60–230 keV/m) over the course of their range, with the bragg peak occurring at the end of the route range where it increases to three times the initial value. Most alpha particles also produce gamma rays. But because of technical restrictions, clinical settings have not yet used treatment planning or post-therapeutic imaging employing alpha particles [19, 20].

Additionally, intracellular buildup of the particles causes multiple clusters of DSBs in target cells and doublestrand breaks (DSBs) in DNA, rendering cellular repair mechanisms ineffective. Due to the particle deposit energy per unit travel length being 1500 times more than β-particles, α-particles have a substantially higher cytotoxicity than β--particles. The physical and radiobiological properties of alpha and beta radiation are listed in table 4. Additionally, because particles travel very quickly, less healthy tissue nearby is harmed. It has been established that the particle radiation is unaffected by the level of cell oxygen [21].

The FDA approved radium-223 dichloride (Xofigo) in 2013 as a particle emitter for treating bone discomfort in prostate and breast cancer patients. Osteoblasts and osteoclasts nearby may experience irreparable DNA double-strand breaks as a result of the emission energy of ^{223}Ra, which is harmful to the nearby cells and prevents the production of aberrant bone. Another alpha particle gaining interest is ^{225}Ac, the parent of ^{213}Bi, which has a half-life of 9.9 days and is considered to be relatively long-lived [21, 22].

Table 1.5. Comparison Physical and radiobiological properties of alpha and beta radiation

Properties	Alpha radiation	Beta Radiation
Tissue range (µm)	20 - 80	2000 - 11500
Linear energy transfer (keV/µm)	~100	~0.3
Decay behaviour	One step and multiple alpha decays	One-step decay to stable nuclide
Radioisotopes	^{177}Lu, ^{131}I, ^{90}Y	^{225}Ac, ^{213}Bi, ^{211}At

This thesis consists of 5 chapters complete with acknowledgments, bibliography, and research achievements.

- Chapter 1: Introduction
- Chapter 2: The bifunctional chelates (BFCs) in radiopharmaceutical applications.
- Chapter 3:   DFT Calculation method for predicting formation constant of complex.
- Chapter 4: Evaluation of 3p-*C*-NETA-TATE as a potential theranostic agent
- Chapter 5: Conclusion and research scheme to be developed.

Chapter 2

The concept of bifunctional chelates (BFCs) in radiopharmaceutical applications

2.1. Introduction

The proper chelator must be matched with a specific radiometal. It is critical to assess crucial aspects of the metal-chelate complex that are relevant to the design of radiopharmaceuticals, such as thermodynamic stability, kinetic inertness, and complexation kinetics. The total electric charge of the metal-chelate complex should also be taken into consideration since it may affect how the radiopharmaceutical is distributed in the body. Due to its relative size to the targeting vector, the metal-chelate complex plays a substantial impact in the overall pharmacokinetic behavior of the system when radiopharmaceuticals are connected to peptides, small molecules, or antibody fragments.

There are two groups of common ligands used in radiopharmaceuticals: acyclic (open chain) and macrocyclic (closed chain). However, recent reports in the literature show good examples of acyclic chelators that exhibit both high thermodynamic stability with a specific metal and excellent kinetic inertness in vitro. Typically, acyclic chelates are less kinetically inert than macrocyclic complexes, even when thermodynamic stability (log K_{ML}) is comparable. For shorter-lived isotopes, acyclic chelators often have quicker metal-binding kinetics compared to macrocyclic equivalents [23, 24].

Even though each metal has a unique coordination chemistry, a limited number of standard chelators are employed across a broad variety of radiometals. For instance, although having less than ideal characteristics with many metals, the tri- and tetraaza-based amino carboxylate macrocyclic chelators NOTA (N_3O_3), DOTA (N_4O_4), and acyclic chelator DTPA (N_3O_5) have been frequently used in radiolabelling studies. Due to the availability of their bifunctional counterparts in commerce, their popularity in radiochemistry may be due to convenience rather than a metal's "best fit". In an effort to

increase tumour-to-background ratios by preventing radionuclide loss in vivo, the recent trend is toward metal-specific chelators with quick radiochemical labeling under mild conditions, high thermodynamic stability, and kinetic inertness.

2.2. Acyclic Chelators
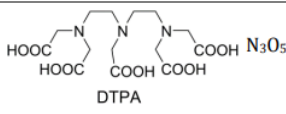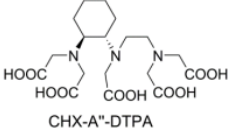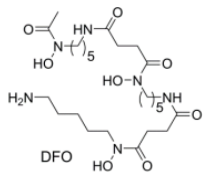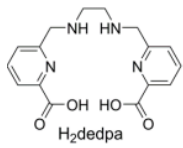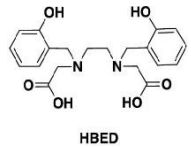
The two most often used acyclic chelates in radiopharmaceutical chemistry are EDTA (N_2O_4) (ethylenediaminetetraacetic acid) and DTPA (N_3O_5) (diethylenetriaminepentaacetic acid). A number radiometals have been labeled using DTPA, including Cu(II) (CN 6, log K_{ML} = 21.4), Ga(III) (CN 6, log K_{ML} = 25.5), In(III) (CN 7, log K_{ML} = 29.5), Y(III) (CN 8, log K_{ML} = 22.0), and Zr(IV) (CN 8, log K_{ML} = 35.8) [25]. It is an excellent option for creating stable of formation constant metal-ligand complexes (log $K_{ML)}$ with bigger hard acidic cations due to its large binding sphere and hard oxygen donor set, and specific coordination number (CN). In three FDA-approved radiopharmaceuticals (^{111}In-based agents OctreoscanTM and ProstaScint®, and ^{90}Y-based agent Zevalin), DTPA derivatives have been effectively included, and it is the chelate in the most often prescribed Gd-DTPA for MRI agent Magnevist[TM]. More recently, the DTPA chelate CHX-A"-DTPA (N_3O_5), which has been improved, has demonstrated tremendous promise for the isotopes of ^{111}In, ^{90}Y, and [213]Bi [26, 27].

Desferrioxamine, often known as DFO (O_6), is an acyclic chelator widely used in iron chelation therapy; It has a terminal primary amine that can be utilized for conjugation to biomolecules and three hydroxamate groups for chelating metals. Due to the comparable properties of high spin Fe(III) and Ga(III), DFO also creates gallium complexes with high thermodynamic stability that have been beneficial for conjugating to peptides and other small molecules [28]. The capacity of DFO to label Zr(IV), the most common choice for zirconium radiochemistry, is one of its applications. It has been shown that the suggested $[Zr(DFO)(H_2O)^2]^+$ combination has excellent in vitro stability (no more than 2% demetallation following seven days in serum) [29]. On the other hand, new small animal PET experiments using an [89]Zr-DFO-antibody show instability in vivo as seen by increased [89]Zr uptake in bone [30].

H$_2$dedpa (N$_4$O$_2$) (1,2-bis{[[6-(carboxy)pyridine-2-yl]methyl]amino}-ethane) is the ligand that can bind with divalent metals Pb(II), Cd(II), and Zn(II) [31, 32]. It has since been shown that H$_2$dedpa has extraordinarily high thermodynamic stability with Ga^{3+} (log K$_{ML}$ = 28.1) and has been repurposed for Ga(III) complexation. It quantitatively identifies gallium isotopes at high specific activities in 10 minutes at room temperature. In addition, [^{68}Ga(dedpa)] + displayed good kinetic inertness in vitro and in vivo, maintaining up to 97% intact for two hours when incubated with excessive apotransferrin [24].

The acyclic chelator, HBED, which has two pendant phenol arms and is based on an ethylenediaminetetraacetic acid (EDTA)-type framework, has various structural features (N and O donor atoms, possible hexadentate coordination environment) that make it a perfect chelator for Ga^{3+}. In the 1960s, the first description of the chelator synthesis was made. Ga^{3+} complex that results from this reaction is very thermodynamically stable (log1 = 38.51) [33].

Table 2.1. Highlights of commonly used acyclic chelator, and thermodynamic formation constants (log K$_{ML}$)

Chelator	Native Donor Set	Metal Ions (log K$_{ML}$)
DTPA	N$_3$O$_5$	Cu(II) (21.4); Ga(III) (25.5); In(III) (29.5); Y(III) (22.0); Zr(IV) (35.8); wBi(III) (35.6)
CHX-A''-DTPA	N$_3$O$_5$	In(III) Bi(III) Ac(III) Lu(III) Y(III)
DFO	O$_6$	Ga(III) (28.6)8 Zr(IV)
H$_2$dedpa	N$_4$O$_2$	Ga(III) (28.1)
HBED	N$_2$O$_4$	Ga(III) (38.5)

2.3 Macrocyclic Chelators

NOTA (1,4,7-triazacyclononane-1,4,7-triacetic acid) and DOTA (1,4,7,10-tetraazacyclododecane1,4,7,10-tetraacetic acid), two widely used tri- and tetraaza-based amino carboxylate macrocyclic chelators, as a group to their bifunctional derivatives, these standards constitute a group of "gold standards" that have been widely applied to the labeling of numerous radiometals for diagnostic and therapeutic purposes. The pendant carboxylic acid arm of NOTA and DOTA has the potential to be employed in a conjugation technique to create a peptide bond with a biomolecule. By using a direct strategy, the chelators' natural donor-ability and binding sphere are changed. Additionally, a second conjugation moiety (p-SCN-Bz) is introduced at a site that would minimize the impact on the ligand's capacity to bind to metals (to generate p-SCNBz-DOTA or p-SCN-Bz-NOTA) or an additional carboxylic pendant arm is added for forming NODASA (1,4,7-triazacyclononane-1-succinic acid-4,7-diacetic acid) [34, 35].

The smaller of the two binding pockets belongs to NOTA (N_3O_3), which is most frequently employed for gallium(III) isotopes (log K_{ML} = 31.0) and is becoming more widely used for copper(II) isotopes (log K_{ML} = 21.6), where it combines with each to create hexadentate complexes. Additionally, the [Ga(NOTA)] complex has a very high acid dissociation stability. Given its near-quantitative room-temperature labeling of gallium isotopes and the excellent in vivo stability of the resultant complex, NOTA has gained special appeal for Ga^{3+} [36].

DOTA as a gold standard is a 12-membered macrocycle which has octa dentate coordination with 4 tertiary amine nitrogen donors, and 4 carboxylic acid pendant arms. This ligand has been widely used as a stable chelator of tri positive radiometals such as $^{68}Ga^{3+}$, $^{111}In^{3+}$, $^{177}Lu^{3+}$, $^{86/90}Y^{3+}$, and $^{44/47}Sc^{3+}$, and is an important chelator of a series of compounds approved by the FDA for the diagnosis (^{68}Ga-DOTA-TATE), and treatment (^{177}Lu-DOTA-TATE) of somatostatin receptor positive neuroendocrine tumors [37, 38]. ^{68}Ga (log K_{ML} = 21.3), $^{86/90}Y$ (log K_{ML} = 24.3), ^{111}In (log K_{ML} = 23.9), ^{177}Lu (log K_{ML} = 25.5), and the divalent nuclide ^{64}Cu (log K_{ML} = 22.3) are some of the trivalent radiometals that DOTA (N_4O_4) and its derivatives form stable complexes with. DOTA also can be used as a chelator for ^{213}Bi and ^{225}Ac, although labeling must be done at high temperatures

(80–95°C) to get a high radiochemical conversion [39-41]. Ideally, radiolabeling can be performed rapidly (<20 min) at room temperature thereby facilitating routine clinical use and minimizing radiolytic damage to heat-sensitive antibody vectors.

In addition, TCMC (N_4O_4) (1,4,7,10-tetraaza-1,4,7,10-tetra-(2-carbamoyl methyl)-cyclododecane), an N,N,N,N-tetraamide analogue of DOTA, has better stability with Pb(II) isotopes in vitro and in vivo than DOTA does, and is the preferred chelate in a clinical trial for [212]Pb. Pb(II) is completely encapsulated by TCMC, which also forms an octadentate complex with 4 nitrogen and 4 amide oxygen donors [42-44].

In the family of macrocyclic chelators for gallium, TRAP (formerly known as PrP9) (N3O3) (1,4,7-triazacyclononane phosphinic acid) is a recent member; it is constructed from a NOTA-type structure, but the carboxylic acid arms have been replaced with phosphinic acid arms. The ability of TRAP to integrate ^{68}Ga almost quantitatively (>95% RCY) at low concentrations in even strongly acidic conditions in 5 minutes at 60 °C is demonstrated by their strong thermodynamic stability with Ga(III) (log K_{ML} = 26.2). Furthermore, the three carboxylic pendant arms connected to the phosphinic acids offer a practical method for the insertion of three focusing on groups via a peptide bond conjugation technique [45].

For Cu(II) radiopharmaceuticals, the tetraazamacrocycle TETA (N_4O_4) (1,4,8,11-tetraazacyclotetradecane-1,4,8,11-tetraacetic acid) has been used extensively. The thermodynamic stability of Cu(II) is comparable to that of TETA and DOTA (log K_{ML} = 21.9 and 22.3, respectively), despite the fact that [Cu(TETA)]$^{2-}$ complexes are less kinetically active than [Cu(DOTA)]$^{2-}$ yet nevertheless exhibit radiocopper loss *in vivo* [30, 47]. The cross-bridged analogue CB-TE$_2$A (N_4O_2) (1,4,8,11-tetraazabicyclo[6.6.2]hexadecane-4,11-diyl)diacetic acid) demonstrates significantly increased stability of copper complexes to enhance the stability of the TETA framework; However, labeling CB-TE$_2$A with Cu(II) isotopes necessitates intense heating (>90 °C) and lengthy reaction periods (1 h), which prevents its use in biomolecules that are thermally sensitive [46].

The most recent addition to the class of ligands used for radiocopper labeling is the sarcophagine type bifunctional chelators (N_6) (sarcophagine = Sar = 3,6,10,13,16,19-

hexaazabicyclo[6.6.6]icosane), but have also been assessed for [68]Ga. At room temperature and in a matter of minutes, sarcophagines can quantitatively label micromolar quantities of [64]Cu. Additionally, the [Cu(Sar)] complexes have strong in vitro kinetic inertness (>98% intact after 4 hours) against mouse serum. These features make Sar cages a promising framework for the integration of thermally sensitive biomolecules into copper-radiopharmaceuticals. In contrast, ^{68}Ga labeling takes 30 minutes of heating at 85°C [47, 48].

HEHA (1,4,7,10,13,16-hexaazacyclohexadecane1,4,7,10,13,16-hexaacetic acid), a large 12-coordinate (N_6O_6) ligand, has been studied largely for radiolabeling of the big radiometal [225]Ac, and many antibodies have been effectively conjugated with it. After 30 minutes of radiolabelling with [225]Ac at 37 °C, RCYs of 60-85% are obtained. Early time points showed the bioconjugates to be sufficiently stable in bovine serum at 37 °C; However, further time points indicate that over a third of the [225]Ac-HEHA-bioconjugate decomposed or was transchelated with serum proteins [49, 50].

3p-*C*-NETA ({4-[2-(bis-carboxy-methylamino)-5- (4-nitrophenyl)-entyl]-7-carboxymethyl-[1,4,7]tri-azo nan-1-yl} acetic acid; a ligand has an extended propyl chain that is employed to bind the NETA backbone and the essential p-NO2 benzyl group for conjugation to antibodies. The additional alkyl spacer was proposed to increase complexation kinetics by reducing steric hindrance in the complex formation of the ligand with a metal. Studies have been reported that 3p-C-NETA to be a promising chelator for radiolabeling reaction kinetics with ^{90}Y, ^{177}Lu, and [161]Tb [51, 52].

3p-*C*-DEPA (1, 2- [(carboxymethyl)] [5-(4-nitrophenyl-1-[4, 7, 10-tris(carboxymethyl) -1, 4, 7, 10- tetraazacyclododecan-1-yl]pentan-2-yl)amino]acetic acid); Ligand with 10 electron donors for complex formation, has a larger cavity than 3p-*C*-NETA. Decadendate 3p-*C*-DEPA was reported to rapidly complex in 1 min with ^{90}Y and ^{177}Lu with radiolabeling efficiencies of 89% and 94%, respectively [53].

Table 2.2. Highlights of commonly used macrocyclic chelator, and thermodynamic formation constants (log K_{ML})

Chelator	Native Donor Set	Metal Ions (log K_{ML})
NOTA	N_3O_3	Cu(II) (21.6); Ga(III) (31.0); In(III) (26.2)
DOTA	N_4O_4	Cu(II) (22.3); Ga(III) (21.3); In(III) (23.9); Y(III) (24.4); Lu(III) (25.5);4 Zr(IV); Ac(III)
TCMC	N_4O_4	Pb(II)
TRAP ($R = CH_2CH_2COOH$)	N_3O_3	Ga(III) (26.2)
TETA	N_4O_4	Cu(II) (21.9); Ga(III) (19.7); In(III) (21.9); Y(III) (14.8); Lu(III) (15.3)
Sar derivatives	N_6	Cu(II); Ga(III)
HEHA	N_6O_6	Ac(III)
3p-C-NETA	N_3O_5	Y(III); Lu(III); Bi(III)

3p-C-DEPA
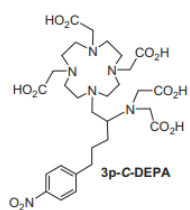
N_5O_5

Lu(III); Ac(III); Bi(III)

Chapter 3

DFT Calculation method for predicting formation constant of complex

3.1 Introduction

The most popular technique for predicting the characteristics of molecules is density functional theory (DFT). Due to the consistency of DFT results, the fields of chemistry and materials science have seen an increase in application [54, 55]. DFT analysis has been crucial for comprehending quick reaction processes and has been used to compute the electronic structure of molecules largely made of organic components or molecules containing transition metals [56, 57]. A method based on a single-configuration approach cannot describe a virtually degenerate electron state for the latter by using a multi-reference character. Recent DFT research, however, has solved this issue and provided accurate results on metal or organometallic clusters. The spectrum and geometry of this interaction model have been effectively explored with DFT study [58, 59].

DFT has been effectively applied to the molecular modeling and investigation of metal groups, including actinides, utilizing a variety of functional and basis set options. Many metal complexes, including transition metals and larger lanthanide and actinide complexes, have been shown to have formation constants and ligand binding free energies that can be precisely calculated using DFT [60, 61].

Condensed-phase formation constants are frequently determined using various thermodynamic cycles. To calculate the solvation free energy and related thermodynamic constants, the solute geometries are optimized in the gas phase before being solvated. In the continuum approach, the interactions (long- and short-range) between the solute and solvent are approximated by creating the molecular cavities of solutes within a dielectric continuum. The free energy of solvation (ΔG_{solv}) is influenced by the electrostatic

interactions (electronic polarization) between the molecular cavity's charge density (solute) and the dielectric continuum's induced surface charge polarization (solvent) [62, 63].

The advantages of radionuclides that release α-particles have made TAT a promising approach of cancer treatment. The α particles can deliver their energy at a much shorter distance, resulting in selectivity for targeted cancer cells and minimizing damage to nearby healthy cells. Moreover, the LET energy of the alpha particles which is significantly more effective in causing lethal DNA double strand breaks in killing cancer cells compared to the lower-LET β particles [64-67].

^{225}Ac^{3+} and ^{213}Bi^{3+} are promising options for using radioisotopes with high LET instead of low LET beta-emitting radioisotopes like ^{90}Y and ^{177}Lu [68]. ^{225}Ac ($t_{1/2}$ = 9.9 d, Eα = 5.8 MeV) has a large energy because it has the property of four α particles which will decay, this condition provides a high cytotoxic potential. Its half-life is ideal for obtaining in vivo circulation of macromolecular targeting vectors such as antibodies [69, 70]. Promising results in the therapy of metastatic castration-resistant prostate cancer with ^{225}Ac-PSMA-617 have led researchers to focus on developing potential clinical applications for α-therapy [71]. ^{213}Bi ($t_{1/2}$ = 45.6 min, Eα = 8.4 MeV) emits one α particle, easily obtained by ^{225}Ac/^{213}Bi generator [77]. The half-life of 45.6 min can be used optimally with small molecule targeting vectors, making it especially useful with radiolabeled systems that differ from ^{225}Ac [72, 73].

The formation of metal complexes and bifunctional ligands with high thermodynamic stability and fast radiolabeling kinetics under mild conditions is urgently needed to minimize toxic side effects related to the biological deposition of the radionuclide [74, 75]. The increased attention of TAT has contributed to the development of new chelating agents since the stable of the radionuclide in vivo is a crucial component of targeted radiation therapy [76].

DOTA as a gold standard is a 12-membered macrocycle which has octa dentate coordination with 4 tertiary amine nitrogen donors, and 4 carboxylic acid pendant arms. This ligand has been widely used as a stable chelator of tri positive radiometals such as ^{68}Ga^{3+}, ^{111}In^{3+}, ^{177}Lu^{3+}, $^{86/90}$Y^{3+}, and $^{44/47}$Sc^{3+}, and is an important chelator of a series of

compounds approved by the FDA for the diagnosis (^{68}Ga-DOTA-TATE), and treatment (^{177}Lu-DOTA-TATE) of somatostatin receptor positive neuroendocrine tumors. DOTA also can be used as a chelator for ^{213}Bi and ^{225}Ac, although labeling must be done at high temperatures (80–95°C) to get a high radiochemical conversion [77]. Ideally, radiolabeling can be performed rapidly (<20 min) at room temperature thereby facilitating routine clinical use and minimizing radiolytic damage to heat-sensitive antibody vectors [78, 79]. The kinetic stability of ^{225}Ac-DOTA complexes has been questioned by various investigations since they show that ^{225}Ac is degraded from DOTA both in vitro and in vivo [86]. This drawback indicates that DOTA is not the best chelator for ^{225}Ac in TAT applications and emphasizes the requirement for better chelating scaffolds for ^{225}Ac. However, the development of ligands for metals with large ionic radii, such as Ac^{3+} (1.22 Å) and Bi^{3+} (1.03 Å), is an important highlight and a challenge, because they have a weak charge density, so that the electrostatic interaction strength with the donor atom of the ligand is weak [80].

3p-*C*-NETA ({4-[2-(bis-carboxy-methylamino)-5- (4-nitrophenyl)-entyl]-7-carboxymethyl-[1,4,7]tri-azo nan-1-yl} acetic acid; a ligand has an extended propyl chain that is employed to bind the NETA backbone and the essential p-NO2 benzyl group for conjugation to antibodies. The additional alkyl spacer was proposed to increase complexation kinetics by reducing steric hindrance in the complex formation of the ligand with a metal. Studies have been reported that 3p-C-NETA to be a promising chelator for radiolabeling reaction kinetics with ^{90}Y, ^{177}Lu, and ^{161}Tb [76, 81].

3p-*C*-DEPA (1, 2- [(carboxymethyl)] [5-(4-nitrophenyl-1-[4, 7, 10-tris(carboxymethyl) -1, 4, 7, 10- tetraazacyclododecan-1-yl]pentan-2-yl)amino]acetic acid); Ligand with 10 electron donors for complex formation, has a larger cavity than 3p-*C*-NETA. Decadendate 3p-*C*-DEPA was reported to rapidly complex in 1 min with ^{90}Y and ^{177}Lu with radiolabeling efficiencies of 89% and 94%, respectively [82].

In this study, we report the radiolabeling and in vitro stability studies of ligands 3p-C-NETA, and 3p-*C*-DEPA labeled with radionuclides (Lu^{3+}, Ac^{3+}, and Bi^{3+}), and DOTA as a benchmark (**Figure 3.1**). We also perform DFT (density functional theory) calculations to evaluate the thermodynamic and kinetic stability of the complex formed.

20

We use M06-HF/6-311G(d) as the functional/basis sets by applying the continuum solvation model SMD (solvation model density) and COSMO (conductor-like screening model). The solvation model is used as a method of approaching radiosynthetic conditions and biodistribution of radiopharmaceutical compounds based on the stability of the ligand complex.
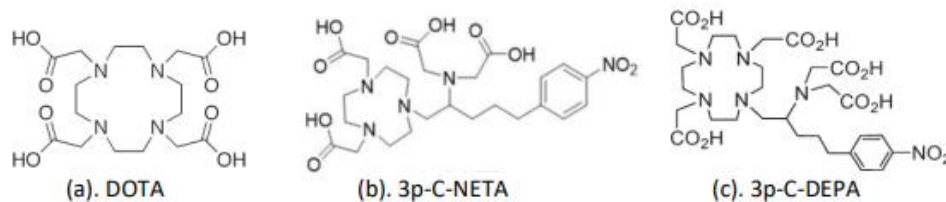
Figure 3.1. (a). DOTA; coordination number= 8; (b) 3p-*C*-NETA; coordination number= 8; (c) 3p-*C*-DEPA; coordination number= 10.

In this DFT study, we also calculated the formation constant for labeling natural products (genistein) with technetium-99^m using direct methods. The development of radiopharmaceuticals from natural products is still rarely the main research focus. The rationale behind choosing these compounds is their potential as template molecules for the creation of innovative radiopharmaceuticals that can identify and/or treat human diseases We tried to explore the natural product-based radiopharmaceuticals, by radiolabeling genistein with several radioisotopes and obtained high RCC results, including with Iodine-131 (RCC 95.02 ± 0.76%), and Technetium-99m (RCC 95.43% ± 0.85%) [83].

Genistein as an isoflavone compound has an important role in the mechanism of Selective estrogen receptor modulators (SERMs) because it has a high affinity for ERβ in target tissues and resist stimulation of the breast, bone, and endometrium. Genistein has potential as a specific ligand for labeling with technetium-99m, making it a potential target or prognostic marker of breast cancer.

Genistein is an isoflavones compound that is abundantly found in soybean seeds with the chemical name [5,7-dihyroxy-3-(-4-hydroxyphenyl)-4H-1-benzopyran-4-one], shown to be potentially specific in the treatment of certain types of breast tumors. Genistein reportedly exhibits strong affinity for human estrogen receptor beta. Selection of alternative treatments and predictive factors for breast cancer prognosis that is

currently widely used include estrogen receptor-positive (ER+), carcinoembryonic antigen (CEA), progesterone receptor (PR), human epidermal growth factor receptor 2 (HER2), urokinase plasminogen activator (uPA), plasminogen activator inhibitor 1 (PAI-1). The evaluation of clinical variables, such as nodal involvement, tumor size, histological type, tumor grade and surgical margins. The active ER signal stimulates cell proliferation and accounts for 75% of all diagnosed breast cancers.

3.2 Computational Details

3.2.1 Thermodynamic Cycle for Determining Formation constants

A formation constant in coordination chemistry is an equilibrium constant for the formation of a complex in solution. It is also known as a formation constant or binding constant. In this study, we focused on the formation of 1:1 complexes by the binding of ligands (3p-*C*-NETA, 3p-*C*-DEPA, and DOTA) to the metals. Calculation of the formation constant K_1 from the 1:1 complex/ligand ratio at equilibrium conditions $M + L \rightleftharpoons ML$ is related to the change in the Gibbs energy of the reaction occurring in solution, ΔG_{aq}. The strength of the metal-ligand interaction is quantified by individual log K_1 values, and the difference between the log K_1 values of two metal ions indicates the degree of selectivity.

$$M + L \rightleftharpoons ML \qquad K1 = \log \frac{[M][L]}{L} = \frac{-\Delta G_{aq}}{2.303\ RT} \qquad (R_1)$$

The reference for calculating ΔG_{aq} is guided by the thermodynamic cycle shown in Figure 2.
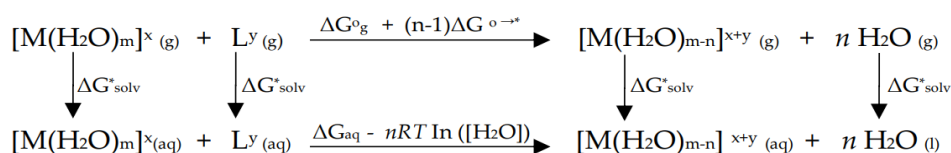
Figure 3.2. Thermodynamic cycle used to calculate ΔG_{aq}.

The free-energy changes of the metal and ligand bindings in the gas phase are represented in this process by the symbol ΔG°_{g}, where ΔG^{*}_{solv} indicates the free energy

needed to solvate 1 mol of solute from its gaseous state into an aqueous phase. The equation calculates the value of $\Delta G°_g$ for normal ideal gas conditions at 1 atm (24.46 mol/L) to 1 M (1 mol/L).

$$\Delta G^{o \rightarrow *} = -T\,\Delta S^{0 \rightarrow *} = RT\,\text{In}\,(Vo/V*) = R.T.\text{In}\,(24.46)$$
$$= 1.89 \text{ kcal/mol (T = 298.15 K)}$$

It is essential for carrying out correction computations. When pure solvent H2O(l) is chosen as the reference state for the solvent, the state of the system is represented by $G_{aq}* = G_{aq}* + RT \ln([H_2O])$. The free-energy change required to move a solvent from a standard-state solution-phase concentration of 1 M to a standard-state pure liquid, 55.34 M, is calculated by RT ln([H2O]) = 2.38 kcal/mol [84].

3.2.2 DFT calculations

In this work, we studied the complexes formed between Lu^{3+}, Ac^{3+}, and Bi^{3+} metals with 3p-*C*-NETA and 3p-*C*-DEPA ligands and using DOTA as a benchmark. All geometry optimizations and frequency calculations were performed in the gas phase with M06-HF as density functionals and 6-311 G(d) as basis sets. The frequency calculation data is used to compute the overall adjustment for enthalpy and entropy at T = 298.15 K as well as to verify the geometric structure with the lowest energy on the potential energy surface. To determine the gas phase free energy for each structure and the differences $\Delta G°g$, these results will be combined with the total energy DFT.

This computational chemistry method was started by calculating the chemical parameters of the genistein ligand structure, including the analysis of NPA (natural population analysis), Natural Bond Orbital Analysis (NBO), and frontier molecular orbitals by a Small Highest Occupied Molecular Orbital-Lowest Unoccupied Molecular Orbital (HOMO-LUMO). Ligands will coordinate with the core (Tc^{4+} core) providing the most stable structure with six-coordinate. This structure is designed with the oxidation stability of technetium in mind and provides a stable pharmacokinetic profile of the geometric complex [20]. Structural optimization was carried out on $[Tc(H_2O)_6]^{4+}$, [genistein]$^{1-}$ ligand, and complex $[Tc(IV)(genistein)(H_2O)_4]^{3+}$ complex. Optimization and frequency of each structure were done using Gaussian 16.0 software. In this study, we

focus on predicting the thermodynamic stability of the formation Tc(lV) complexes with genistein ligands for a ratio of 1: 1. The calculation of metal/ligand complexes 1:1 at equilibrium conditions $M + L \rightleftharpoons ML$, where the value of the formation constant K_1 for the reaction in solution correlates with the change in free energy - Gibbs, ΔGaq

3.2.3 Conceptual DFT-Based Characteristic

The DFT-based structural characteristics (chemical hardness, η, and softness, S) were calculated using the following equations:

$$\eta = \frac{(IP-EA)}{2} \qquad\qquad S = \frac{1}{2\eta} \qquad\qquad (R_2)$$

where IP (ionization potential), and EA (electron affinity), were obtained from DFT calculations for the frontier orbital energies, HOMO and LUMO [85].

3.3 Results and Discussion

3.3.1 DFT Calculation

3.3.1.1. DFT calculation of complexes metals (Lu^{3+}, Ac^{3+}, and Bi^{3+}) with ligands (DOTA, 3p-*C*-NETA, and 3p-*C*-DEPA)

We performed DFT calculations to determine formation constant calculations of complexes formed from metals (Lu^{3+}, Ac^{3+}, and Bi^{3+}) with 3p-*C*-NETA and 3p-*C*-DEPA ligands, respectively. The DOTA complex of each radiometal used as a benchmark. Ligands will form complexes with metals with oxidation stability in Lu^{3+}, Ac^{3+}, and Bi^{3+} respectively. The DFT analyses of the Ac^{3+} ion with 4–11 water molecules showed that $[Ac(H_2O)_9]^{3+}$ is the most stable in both the gas phase and the aqueous phase (COSMO model), which served as the inspiration for this choice of coordination number (CN) 9 [86]. Furthermore, the selection of CN from Lu^{3+} was based on a geometric stability study of the water exchange process for Lu^{3+} ions. Several studies reported that Lu^{3+} has a CN 9 in the study of the stability of the geometry and crystal structure [87, 88].

Bi^{3+} demonstrates a very varying coordination number (3–10) and frequently an irregular coordination geometry, based on the characteristics of the donor atoms, the solvent, and indeed the polydentate ligand. Furthermore, bismuth (III) hydrolyzes relatively quickly in aqueous solutions even in very acid solutions. As a result, the development of hydrolysis products makes it challenging to research bismuth (III) complexes in aqueous solutions. In addition, other studies have proposed Bi^{3+} with 6 coordinates with pentagonal pyramidal geometry and the directionality of the stereochemically active 6s2 lone pair [74, 89].

The DFT was performed with Gaussian 16 to complete the calculations, and the ChemCraft software was used to visualize the structure graphically. In this study, the DFT calculation uses the new hybrid meta-exchange-correlation full-Hartree–Fock (M06-HF) as a hybrid density functional with consideration of its advantages in calculating main group thermochemistry, thermochemical kinetics, noncovalent interactions, excited states, and transition elements [90]. in addition, MO6-HF has good self-interaction error (SIE) in Density Functional as indicated by the small average mean unsigned errors (average MUE) (in kcal/mol), when compared to the Perdew-Burke-Ernzerhof (PBE) functional and Becke, 3-parameter, Lee-Yang-Parr (B3LYP) that are commonly used [91].

We performed a DFT calculation by calculating the absolute formation constant of the ligands and complexes formed. **Figure 3.3** shows the representative equilibrium geometries of Actinium ions with nine coordinated water molecules, ([Ac(H$_2$O)$_9$]$^{3+}$, [3p-*C*-DEPA]$^{5-}$), and their complex, [Ac(3p-*C*-DEPA)].

[Ac(H$_2$O)$_9$]$^{3+}$ [3p-C-DEPA]$^{5-}$ [Ac(3p-C-DEPA)]$^{2-}$
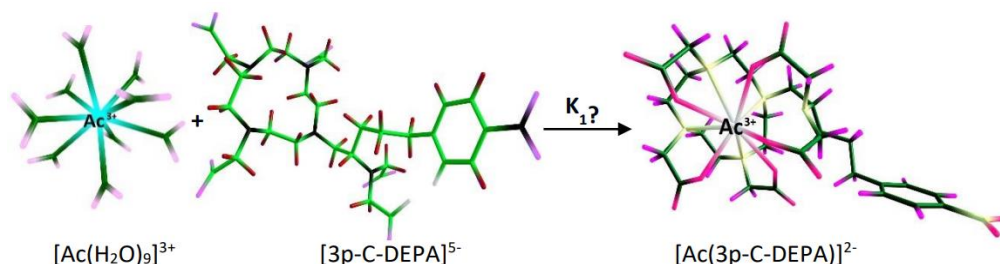
Figure 3.3. Representative equilibrium geometries of [Ac(H$_2$O)$_9$] $^{3+}$, [3p-*C*-DEPA]$^{5-}$), and their complex [Ac(3p-*C*-DEPA)]$^{2-}$

Based on the results of the complex geometry optimization, the classification of the atoms in the Ligands-radiometal ion complex was performed with the objective of

making the interpretation of the data more clear, by evaluating at the atoms' positions, connectivity, and various functional groups, which impact how their chemical environments differ from one another (**Figure 3.4**).
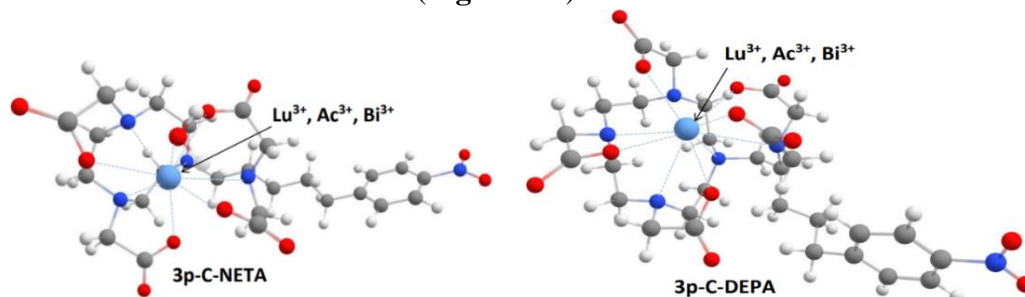
Figure 3.4. Conformation structure of the 3p-*C*-NETA, and 3p-*C*-DEPA-radiometal ion complexes. Intermolecular distances between nearby heteroatoms and radiometal ions are illustrated in the figures by blue dots., where the geometric structure of 3p-*C*-NETA and 3p-*C*-DEPA is the result of geometry optimization.

We determined single-point aqueous solvation free energies, ΔG^*_{solv}, using the geometries of the gas phase, and we used both the SMD model and COSMO model to evaluate the electrostatic interaction of a molecule with a solvent. The estimates for absolute formation constants could be further enhanced by using computationally intensive techniques like explicit solvent quantum calculations [92]. The thermodynamic cycle be completed to get the formation constants, $\log K_1$, and the free-energy changes in the aqueous phase, ΔG_{aq}. The systematic errors within the computational methods may be largely cancelled using the deftly planned thermodynamic cycles [93].

DFT calculations for the formation constants ($\log K_1$) of the radiometal-ligand complex in the gas phase, and the solvation models (SMD and COSMO) are reported in **Table 3.1**. DFT calculations on the SMD and COSMO models show that 3p-*C*-DEPA has a better formation constant for Ac^{3+}, and Bi^{3+} which has a large ionic atomic radius, slightly lower results compared to Lu^{3+}. In contrast, Lu^{3+} with a smaller atomic radius has a higher the formation constant in complex formation with DOTA, when compared to Ac^{3+} and Bi^{3+}. 3p-*C*-DEPA with the larger macrocyclic cavity and have 10 donors in complexing were significantly more effective at binding Ac^{3+} which has a larger atomic radius than Lu^{3+}. The ionic radius of the metal ion is inversely related to the stability of metal ion complexes of DOTA from a thermodynamic perspective, with bigger metal centers producing less stable complexes.

Table 3.1. Calculated formation constants ($\log K_1$) for the complexes

Metals	Ligands	M06-HF/6-311G(d)		
		$\log K_1$ (Gas)	$\log K_1$ (SMD)	$\log K_1$ (COSMO)
Lu $^{3+}$	[DOTA]$^{4-}$	830.72	41.38	46.13
	[3p-*C*-NETA]$^{4-}$	568.1952	41.26	48.51
	[3p-*C*-DEPA]$^{5-}$	636.69	12.15	12.53
Ac $^{3+}$	[DOTA]$^{4-}$	815.833	22.75	28.17
	[3p-*C*-NETA]$^{4-}$	556.173	22.55	27.71
	[3p-*C*-DEPA]$^{5-}$	637.073	37.77	38.75
Bi $^{3+}$	[DOTA]$^{4-}$	833.525	46.95	48.23
	[3p-*C*-NETA]$^{4-}$	573.155	42.85	47.66
	[3p-*C*-DEPA]$^{5-}$	650.907	35.91	39.56

The 3p-*C*-NETA ligand's formation constant computation reveals that Ac^{3+} has a lower stability of complex formation than Lu^{3+} or Bi^{3+}. This is in accordance with our radiolabeling for Ac^{3+}, ^{225}Ac mildly complexed to 3p-C-NETA in 1 h at a concentration of 5 M (RCC of 72.2 10% at 25 °C), compared to DOTA, which struggled under the same labeling conditions (RCC of 0.6 0.2%). Interestingly, the RCC for 3p-*C*-NETA was not significantly affected when the temperatures were increased to 95 °C. In contrast, radiolabeling for for Bi^{3+} showed that quantitative RCCs could be obtained from 10 M 3p-*C*-NETA at 25° in under 5 minutes as contrast to DOTA's lesser complexation yield (11.0 1.0%). Moreover, the RCC of ^{177}Lu with 3p-*C*-NETA completed in 12 min at 25 °C showed excellent results, as determined by iTLC (RCC of 99.4 ± 0.4%). Octadentate 3p-*C*-NETA with the smaller nine-membered ring was shown to be the most effective chelate in binding the lanthanides [64].

3.3.1.2. DFT calculation of complexes metals Technetium-99m with genistein

All calculations were conducted by implementing DFT as applied to Gaussian 16, and the graphical visualization of structure using ChemCraft program. The optimization of the structure and frequency calculations were performed out in the gas phase. Geometry optimization of each structure and frequency calculations were carried out at M06/6-311+G (d). The frequency calculation aims to verify that all geometric structures have reached the minimum energy conditions from the potential energy surface and to calculate the thermal correction of the enthalpy and total entropy at the ideal gas temperature. The NPA and HOMO-LUMO analysis concluded that O atoms number 2

and 3 are the most potential regions to bond with metal atoms (Tc^{4+}). After obtaining the best structural model of the [Tc(genistein) ($H_2O)_4]^{3+}$ complex, we performed geometry optimization and DFT calculations. The structural model of the complex [Tc(genistein)($H_2O)_4]^{3+}$ calculated by DFT. The representative equilibrium geometries of the technetium ion with six coordinated water molecules, [Tc($H_2O)_6]^{4+}$, [genistein]$^{-1}$ ligand, and their complex [Tc(genistein)($H_2O)_6]^{4+}$ (**Figure 3.5**).
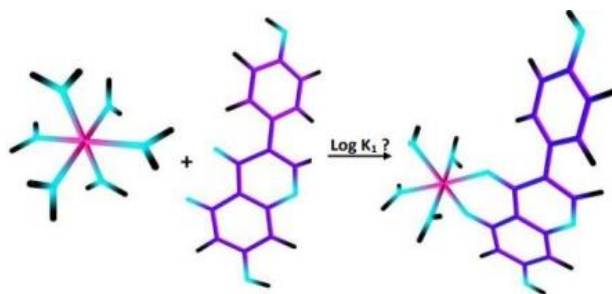
Figure 3.5. Representative equilibrium geometries of the Technetium ion with 6 coordinated water molecules [Tc($H_2O)_6]^{4+}$, [Genistein]$^{1-}$ ligand, and their complex [Tc(lV)(genistein)($H_2O)_4]^{3+}$

DFT computations utilizing computationally demanding techniques like implicit solvent quantum can greatly improve predictions of the absolute formation constants. Finally, in table 3.2, we found that the selection of the basis sets (6-311+G(d)), density functionals (M06), the models for solvation that were chosen (SMD) give the best formation constants (log K_1) at DMSO solvent is 99.0822.

Table 3.2. Formation constants (log K_1) for the [Tc(IV)-genistein]$^{3+}$ complex

Equilibrium	Functional/ Basis Sets	Log K_1 Water	Log K_1 DMSO	Log K_1 Ethanol	Log K_1 Methanol
Tc^{4+} + (genistein)$^{1-}$ ⇌ [Tc(IV) (genistein)]$^{3+}$	M06/ 6-311+G(d)	39.721	99.082	52.316	44.67

The DFT calculation of the [Tc(IV)(genistein)]$^{3+}$ complex was carried out with a thermodynamic cycle designed to largely cancel the systematic error in the calculation of the free energy change in the liquid phase, ΔGaq, and the formation constant, log K_1. The first DFT calculation step is to find the atomic position on the ligand that will bind to the

metal to form the most stable configuration of the complex structure. NPA and NBO analysis of the genistein ligand structure is useful for understanding electron density delocalization, and for measuring intermolecular or intramolecular interactions. This information can ensure the charge transfer in the chelator complex is important because it affects the interaction of the radiometal ion with the ligand. Furthermore, we also performed HOMO-LUMO analysis to provide the information the prediction of the most reactive positions and support the information on which reaction occur in the conjugated system. The results showed that the O-H atomic bond between O-2 and H-28 atoms has the smallest bond order of 0.6497, compared to the bond between O-4 and H-30 (0.7515), and O-5 and H-29 bonds (0.7555), therefore the atomic bond of O-2 and H-28 is the deprotonation location which is the best position for interaction with $[Tc(H_2O)_6]^{4+}$.

A strategy to improve the accuracy of solvation calculations for ions is to include chemically important solute-solvent explicitly into the quantum chemical model. In this study, we used the SMD model (solvation model density) which is a continuum solvation model that can be applied to any charged or uncharged solute in the solvent. M06 of density functionals which has advantages in calculating main group thermochemistry, thermochemical kinetics, noncovalent interactions, excited states, and transition elements. The solute-solvent interaction has a very strong and profound effect on chemical reactivity. Polar protic solvents and dipolar aprotic solvents have an important role in ionic chemical reactions because of their properties that dissolve ionic species such as methanol, dimethyl sulfoxide (DMSO), dimethylformamide (DMF) and acetonitrile. Genistein has good solubility in ethanol, methanol, and DMSO, but poorly soluble in water. DFT calculation of $[Tc(IV)(genistein)]^{3+}$ complex in various solvents showed significant results that the formation of the most stable complex in DMSO solvent, indicated by the highest value of formation constant ($\log K_1$) (99,0873) compared to other solvents

3.3.2 Conceptual DFT-Based Properties

The study of several aspects of pharmacological sciences, such as drug design, has led to the proposal of a number of chemical reactivity descriptors. Density functional theory as a starting point, can calculate the concepts of potential importance of reactivity

descriptors such as chemical potential, electronegativity, hardness, softness, and electrophilicity index. The potential of an atom or molecule to donate electrons is referred to as its ionization potential, whereas its ability to attract electrons is referred to as its electron affinity. Chemical hardness, which is connected to the stability of the chemical system, indicates the resistance to modification in electron distribution. Global softness, which has a connection with the chemical system's reactivity, is the opposite of hardness [94]. Table 2 presents the computed DFT-based values for the complexes' electron affinity (EA), ionization potential (IP), chemical hardness (η), and softness (S).

Table 3.3. DFT-based quantities for radiometal ion (Lu^{3+}, Bi^{3+}, and Ac^{3+}), and the ligands (DOTA, 3p-C-NETA, 3p-C-DEPA) calculated at the M06-HF/6-311G(d) level of theory

System	EA (eV)	IP (eV)	η (eV)	S (eV)
Lu^{3+}	0.801	2.233	0.716	0.698
Bi^{3+}	0.207	1.396	0.594	0.841
Ac^{3+}	0.691	1.725	0.517	0.967
DOTA	-0.401	-0.182	0.109	4.567
3p-C-NETA	-0.245	-0.052	0.096	5.197
3p-C-DEPA	-0.285	-0.103	0.091	5.487
DOTA-Lu^{3+}	0.0705	0.3834	0.227	2.203
3p-C-NETA-Lu^{3+}	0.0034	0.3725	0.184	2.709
3p-C-DEPA-Lu^{3+}	0.0034	0.3473	0.172s	2.908
DOTA-Bi^{3+}	-0.0037	0.2577	0.131	3.825
3p-C-NETA-Bi^{3+}	0.0033	0.2684	0.132	3.772
3p-C-DEPA-Bi^{3+}	0.0036	0.2659	0.131	3.812
DOTA-Ac^{3+}	0.0029	0.3441	0.171	2.931
3p-C-NETA-Ac^{3+}	0.0033	0.3507	0.173	2.878
3p-C-DEPA-Ac^{3+}	0.0034	0.3542	0.175	2.849

For free ion, The DFT calculation demonstrates that for Ac^{3+} compared to Bi^{3+} and Lu^{3+}, a higher ionic radius is observed the lower the chemical hardness, and this is consistent with the findings for the atomic radius of Ac^{3+} is larger than Bi^{3+} and Lu^{3+}. In addition, the DFT-based properties show that 3p-C-DEPA has a lower chemical hardness compared to 3p-C-NETA and DOTA. The hard-soft acid-base (HSAB) concept by Pearson determines how metals interact with their ligands, with "hard" ions interacting most strongly with "hard" ligands and opposite. The chemical hardness of the complex can explain the stability of the complex, where the DOTA complex with radiometal Lu^{3+}

has a higher value and is more stable than Ac^{3+} and Bi^{3+}. Furthermore, 3p-*C*-NETA seems to be very suitable for binding to Lu^{3+} compared to Ac^{3+}, and Bi^{3+}. Therefore, 3p-*C*-DEPA appears to be more stable in binding to Ac^{3+}. Trends in complex stability are provided by changes in EA, IP, softness, and hardness, which are associated to trends in interaction energies and thermodynamic characteristics.

3.4 Conclusion

3p-*C*-DEPA is a suitable chelator for radiometals with large atomic radii such as Ac^{3+} compared with Lu^{3+}, this is supported by good RCC data in mild condition and stability in PBS and Serum. 3p-*C*-NETA showed excellent results on RCC and stability in PBS and HS for Lu^{3+}, and Bi^{3+}. The DFT calculation approach can support and explain the characteristics of each component and the formation constant in the complex formation process.

Chapter 4

Evaluation of 3p-*C*-NETA-TATE as a Potential Theranostic Agent

4.1 Introduction

Surgery is commonly utilized as a kind of treatment for neuroendocrine tumors (NETs). Somatostatin analogues (SSAs) may be used for symptomatic relief or when disease progression is suspected in the majority of NETs because they are indolent and occasionally observed without any active treatment. However, a large number of NETs require systemic therapy since they are either incurable or discovered at an advanced stage involving distant spread. Although SSA is successful in managing symptoms of disease and stabilizing the condition, an objective response is not common [95-97] NET management after SSAs is based on individualized patient treatment, which may include mTOR inhibitors, interferons, tyrosine kinase inhibitors, peptide receptor radionuclide therapy (PRRT), and liver-targeted therapies, and is determined by the extent of the disease, grade of the tumor, stage, and location of the disease [98, 99].

The initial radiopharmaceutical permitted by the FDA for NETs is PRRT with [^{177}Lu]Lu-DOTA-TATE, despite the fact that radiolabelled somatostatin analogue therapy has been used for the past 20 years. The randomized controlled phase III landmark worldwide multicenter open-label NETTER-I study results served as the foundation for the approval, which assessed the effectiveness of [^{177}Lu]Lu-DOTATATE against high-dose long-acting octreotide (LAR) in treating patients with inoperable, advancing, G1-G2 somatostatin receptor-positive midgut NETs [100, 101].

The drawback of ^{177}Lu-DOTATATE therapy is that 26–55% of patients only have disease stabilization, and a sizeable portion, about 18–32%, are refractory to beta radiation. Therapy with ^{177}Lu-DOTATATE. The potential benefits of high LET alpha-

emitting radioisotopes, especially ^{225}Ac and ^{213}Bi, rather than low LET beta-emitting radioisotopes, such as ^{90}Y and ^{177}Lu, have received attention as an alternate solution. The development of ideal chelator for Ac and Bi has progressed, and is a challenge in itself. This is because ^{213}Bi and especially ^{225}Ac have relatively large atomic radii, so a chelator is needed that is able to trap them effectively. Furthermore, precursor evaluation for NETs applications is the next stage.

The most frequently used method for diagnosing NETs in clinical practice is [^{68}Ga]Ga-DOTA-TATE. The development of ^{18}F-labeled radiopharmaceuticals, which provide significant logistical advantages over gallium-68, has led to the development of ^{68}Ga-labeled tracers as an alternative in recent years [102]. Fluorine-18 is technically able to be routinely produced by cyclotrons facilities in large quantities, this is not possible for ^{68}Ga when used with ^{68}Ge/^{68}Ga generators. The production of gallium-68 in cyclotrons could be improved to address this drawback, however, not all cyclotron facilities may be able to implement this solution [103, 104]. Due to the substantially longer half-life of ^{18}F ($T_{1/2}$: 109.8 min) than ^{68}Ga ($T_{1/2}$: 68 min), imaging processes can be prolonged, potentially increasing the rate of lesion identification, and fluorine-18-labeled tracers can be transferred to PET facilities located far away from the location of production. As a result, ^{18}F-labeled radiopharmaceuticals can be produced and quality-controlled centrally and transported to distant hospitals without cyclotrons or radiopharmacies on site [105, 106].

The Al^{18}F-technique combines the benefits of a chelator-based radiolabeling technique with the diagnosis and logistics benefits of fluorine-18. These labeling techniques have shown results with [^{18}F]AlF-NOTA-Octreotide and [^{18}F]AlF-FAPI-74, which are promising examples. The fact that the most common chelators for the Al^{18}F-method, 1,4,7-triazacyclononane-N,N',N'-triacetic acid (NOTA), are pentadentate ligands when conjugated to a vector molecule because one of the three carboxylic arms is utilized for amide bond formation, is a significant disadvantage, is incompatible with prospective therapeutic radionuclides including actinium-225 (^{225}Ac) and bismuth-213 (^{213}Bi), as well as the -emitter lutetium-177 (^{177}Lu). As a result, two distinct precursors are needed to make the diagnostics and therapeutic radiopharmaceuticals [107, 108].

^{177}Lu^{3+}, ^{225}Ac^{3+}, and ^{213}Bi^{3+} still remain chelated with 1,4,7,10-tetraazacyclododecane-1,4,7,10-tetraacetic acid (DOTA), although the fact the use of this chelator has a number of disadvantages. Heat-sensitive vector molecules cannot be used with the normal radiolabeling conditions for DOTA, which require heating at high temperatures (e.g., 30–60 min at 95 °C). Furthermore, it has been demonstrated that the weak kinetic characteristics of DOTA ligands necessitate the use of high concentrations of these compounds to produce quantifiable yields [109].

3p-*C*-NETA ({4-[2-(bis-carboxy-methylamino)-5- (4-nitrophenyl)-entyl]-7-carboxymethyl-[1,4,7]tri-azo nan-1-yl} acetic acid; a ligand possessing both a parent macrocyclic NODA (1,4,7-triazacyclononane-N,N'-diacetic acid) backbone, According to Chong et al., this chelator exhibits promising kinetics and stability for β-emitters like ^{90}Y and ^{177}Lu. It also features a flexible acyclic tridentate pendant arm. ^{90}Y and ^{177}Lu formed a complex with 3p-*C*-NETA in less than five minutes (>95%). In response to these intriguing findings, Kang et al. successfully assessed the stability and pharmacokinetics of ^{90}Y and ^{177}Lu-labeled 3p-*C*-NETA trastuzumab in tumor-bearing mice. Additionally, remarkable labeling kinetics with $^{205/6}$Bi were described, as well as stability investigations of the resultant Bi-complex, suggesting that 3p-C-NETA would be the most suitable chelator for ^{213}Bi [110].

We carried out a preclinical evaluation of 3p-*C*-NETA-TATE, which was created by conjugating the somatostatin analogue (Tyr3)-octreotate with 3p-*C*-NETA, by using DOTA-TATE as a benchmark. In this study, we investigated by evaluating the *in vitro* stability of 3p-*C*-NETA and DOTA-TATE radiocomplexes, Cell Binding and Internalization Studies, Cell Viability Test, Clonogenic Test, and Biodistribution Test.

4.2 Experimental section

4.2.1 Materials

Reagents and solvents: All chemicals and solvents used in this study were obtained from commercial vendors such as Sigma-Aldrich (Bornem, Belgium), Fluka (Bornem, Belgium), Fisher (Doornik, Belgium), and Acros Organics (Geel, Belgium), and were

used without additional purification. DOTA-TATE is obtained from ABX advanced biochemical compounds, Germany.

4.2.2 Radiochemistry

All radioactive tests were conducted in labs with suitable lead block shielding and authorized fume hoods. The Millipore water purification system was used to deionize and purify all the water until it had a resistivity of 18 MΩ cm. Fluorine-18 was obtained locally in a cyclotron (IBA Cyclone 18/9, IBA, Louvain-la-Neuve, Belgium) by irradiation $H_2^{18}O$ with 18-MeV protons. ITM Medical Isotopes GmbH (ITM Group, Garching Munich, Germany) supplied the [^{177}Lu]LuCl$_3$ (0.05 M HCl). Chelex 100 [sodium form (50-100 mesh, Sigma Aldrich)] was used to remove trace metals from all radiolabeling buffers for 15 minutes. Before use, each solution was filtered and gassed. The complexation reactions were performed at 40, 60 and 95 °C for [^{177}Lu]LuCl$_3$. The 3p-*C*-NETA and DOTA-TATE were labeled by [^{177}Lu]LuCl$_3$: (6 MBq, 0.1M NaOAc, pH 4.1), and for 3p-C-NETA-TATE adding [^{18}F]AlF: (4 MBq, 0.1M NaOAc, pH 4.1, in the appropriate buffer solution, and the reaction mixture (V= 1 mL) was incubated for 12 minutes at the desired temperature.

Instant thin-layer liquid chromatography-Silica Gel (iTLC-SG, Varian, Diegem, Belgium) was used in evaluating RCC. Acetonitrile: water (75/25 v/v) was used in an elution chamber to create iTLC-SG papers. Free [^{18}F]AlF and [^{177}Lu]LuCl$_3$ have retention factors (rf) between 0.14 and 0.22. The radiocomplexes have an Rf between 0.91 and 0.94.

4.2.3 *In vitro* stability of 3p-*C*-NETA and DOTA-TATE radiocomplexes

According to a previous description, all radio-synthesized complexes were purified using a Sep-Pak C$_{18}$ Light cartridge from Waters in Eschborn, Germany. Briefly, 100% ethanol and water were used to pre-condition the Sep-Pak C$_{18}$ Light cartridge (5 mL each). After loading the reaction mixture onto the cartridge, the radionuclide was rinsed away with 6–8 mL of water. Using 0.25 mL of 100% ethanol to elute the pure radio-complex, the volume was then diluted with 0.25 mL of 0.9% NaCl to reach 0.5 mL. The solution was incubated at 37 °C with continual slight shaking after 50 µL of the purified radio-

complex was introduced to a 1 mL vial containing either 450 µL of PBS or human serum. For iTLC analysis on 5 µL samples of ^{177}Lu radiocomplexes at specific time periods (10 min, 1, 2, 3, 5, and 7 d), the percentage of intact radio-complexes was calculated.

4.2.4 Cell Binding and Internalization Studies

Binding assay is the method to measures the interaction of the radiolabeled compound to its specific receptor. Internalization was carried out to ensure the amount of radioligand bound to the receptors, at the cell membrane and internalized into the cell [112].

In this study, we set time of incubation; 5, 10, 30, 60, 120, 180, 240, and 3 d). Binding specificity was evaluated using 2 x 10^5 BON-1-SSTR2 cells/well (70-90%) to have 4-5 x10^5 cells. Next, cells were incubated with [^{177}Lu]Lu-3p-*C*-NETA-TATE and [^{177}Lu]Lu-DOTA-TATE alone or in blocking study with excess of octreotide acetate (100 µM) for 60 min. After incubation, cells were washed twice with ice-cold PBS and lysed using 1 M NaOH during 2 x 5 min at RT. To remove the radioactivity bound on the surface of the cells, incubate cells with 0.5 mL glycine-HCl (50 mM, pH 2.8) for 5 min at room temperature. Lyse cells by incubating (3-4 min) and pipetting up and down at least 8-12 times, and then collect cell lysate in "Cell" eppendorf. The radioactivity of the Free ligand, first lysine wash, second lysine wash, lysate were counted in a γ-counter (PerkinElmer 2480 Automatic Gamma Counter, WIZARD$^{2®}$). Data was analyzed using one-way ANOVA with a P-value < 0.05 for significant difference.

4.2.5 Cell Viability Test

Cell viability and/or proliferation rates are reliable measures of a cell's health. Cell health and metabolism can be impacted by physical and chemical factors. These substances may be hazardous to cells by a variety of processes, including enzymatic reactions, protein synthesis suppression, irreversible binding to receptors, degradation of cell membranes, and irreversible binding to receptors. Short-term cytotoxicity and cell viability assays that are affordable, dependable, and reproducible are required to identify the cell death brought on by these processes. In vitro cell viability and cytotoxicity experiment with cultured cells are frequently used for cytotoxicity tests of chemicals and

for drug screening. Assays for determining cell viability and cytotoxicity are based on a variety of cell processes, including nucleotide absorption activity, enzyme activity, cell adhesion, Adenosine Triphosphate (ATP) synthesis, and coenzyme production. experiments employing human cells may be more relevant than some in vivo animal experiments, while in vitro cytotoxicity and/or cell viability assays have several benefits, such as speed, lower cost, and the possibility for automation. However, they have certain drawbacks because they are not technologically developed enough to replace animal testing [113].

MTT assay

One of the most used colorimetric assays for determining cytotoxicity or cell viability is the MTT (3-(4,5-dimethylthiazol-2-yl)-2-5-diphenyltetrazolium bromide) assay. This test measures the activity of mitochondrial enzymes such as succinate dehydrogenase in order to detect the viability of cells in particular. NADH converts MTT in this experiment into a purple formazan. By measuring the absorbance of light at a particular wavelength, this product can be measured. Due to its simplicity, safety, great reproducibility, and widespread use in both cell viability and cytotoxicity assays, this technique is significantly superior to the dye exclusion techniques previously discussed. The redox potential in viable mammalian cells causes the water soluble MTT reagent (3-(4,5-dimethylthiazol-2-yl)-2,5-diphenyltetrazolium bromide) to convert to an insoluble formazan product. After solubilization of the formazan with the included SDS (sodium dodecyl sulfate) reagent, the concentration of the colorimetric probe is determined by an optical density measurement at 570 nm, measurements were carried out with Microplate Readers [114].

In this study, we used CyQUANT MTT Cell Viability Assay Protocol (ThermoFisher), with 22 series of activities: 3 KBq – 150 MBq of each [177Lu]Lu-3p-*C*-NETA-TATE, and [177Lu]Lu-DOTA- TATE

4.2.6 Clonogenic Assay

An *in vitro* cell survival assay based on a single cell's capacity to develop into a colony is known as a clonogenic assay or colony-forming assay. A colony is considered

to have at least 50 cells. In essence, the assay examines each cell in the population to determine whether it has the capacity for "unlimited" cell division. Clonogenic assay, which can also be used to assess the efficacy of other cytotoxic agents, is the preferred technique for determining cell reproductive mortality following exposure to ionizing radiation. The ability to form colonies is only retained by a small portion of the implanted cells. Cells are diluted appropriately before or after treatment and seeded out to form colonies in 1-3 weeks. Colonies can be counted under a stereomicroscope after being fixed with glutaraldehyde (6.0% v/v), stained with crystal violet (0.5% w/v), and fixed. Included is a technique for analyzing radiation dose-survival curves [115].

Clonogenic assay setup

Using this assay, research can be conducted in two fundamentally distinct ways:

(A) Cells are plated before treatment. From a stock culture, cells are taken and plated into (cluster) dishes at the proper dilutions. The treatment of the cells occurs after attachment of the cells to the dishes, which typically takes two hours or longer. The procedure must be carried out prior to cell replication, failing which additional colonies will result from an increase in the number of cells per plate. Immediately following treatment, the plates are put in an incubator and kept there for at least six potential cell divisions. This technique is frequently employed for a fast assessment of the susceptibility of cells to various treatments.

(B) Cells are first treated in dishes and then replated in the proper dilutions, to evaluate clonogenic potential. Replating may be done right away following treatment or it can be delayed to allow for repair procedures. This technique is particularly employed in radiobiological studies to identify possibly fatal- and sublethal damage repair

Plating efficiency and surviving fraction.

The efficiency of plating varies among different cell lines. Untreated cells will form colonies when they are plated as a single-cell solution at low densities of 2–50 cells cm^{-12}. PE measures how many colonies there are in relation to the quantity of cells planted.

$$PE = \frac{no: of\ colonies\ formed}{no: of\ cells\ seeded} \times 100\%$$

The surviving fraction (SF) is the quantity, expressed in terms of PE, of colonies that form after the treatment with cells.

$$SF = \frac{\text{no: of colonies formed after treatment}}{\text{no: of cells seeded x PE}} \text{ x } 100\%$$

In this study, 1×10^3 cells were plated in a 6-well plate. Five different concentrations (0; 0.1; 0.6; 1.3; 1.7 MBq/well) of [^{177}Lu]Lu-3p-*C*-NETA-TATE compared with [^{177}Lu]Lu-DOTA-TATE were added in triplicate. After 0.5, 1, 2, and 5 hours, the different cells were replenished with fresh cell medium. After 12 days of cell culture, cell medium was removed and the cells were washed twice with ice-cold PBS. Colonies were stained with 1 mL of 0.1% crystal violet in a 70% ethanol and 37% formaldehyde solution for 30 min after which the plates were rinsed three times with MilliQ water and subsequently air-dried.

4.2.7 *In vivo* biodistribution of 3p-*C*-NETA-TATE

Biodistribution (BD) studies are performed to determine the distribution and the persistence of the radiopharmaceuticals compound to target and nontarget tissues following direct in vivo administration in animals. Animals are euthanized on the day of the experiment at the moment of maximum radioactivity uptake in the tissue of interest after being injected with the radiopharmaceutical at doses greater than those used for biodistribution studies (37 MBq for rats and 7–8 MBq for mice). Target tissues and blood are collected, to collect plasma samples, blood is centrifuged in tubes that have been heparinized.

In order to get accurate data from a quality assurance system, gamma counter calibration is required. Small levels of radioactivity, such as those found during plasma counting, metabolite analysis, or biodistribution tests, can be measured using a γ counter system. When dealing with radionuclides that generate positrons, a γ counter that can detect activity between 511 and 1022 MeV is required. We evaluated 3p-*C*-NETA-TATE using the Al^{18}F labeling method. Al^{18}F labeling is a relatively novel technique that enables one-step radiofluorination of biomolecules in aqueous solution, including

proteins and peptides. The 3p-*C*-NETA-TATE was successfully radiolabeled with [^{18}F]AlF in an automated AllinOne® with a good radiochemical purity [^{18}F]AlF-3p-*C*-NETA-TATE (>97%).

In this biodistribution study, there is a treatment group with the addition of gelofusine [Braun], which aims to obtain information on reducing the renal retention of radiolabeled peptides and antibody fragments. Radiopharmaceuticals based on hydrophilic peptides are often removed from the body by the kidneys. A radiopharmaceutical's therapeutic efficacy may be hampered if it is retained in the kidneys. The renal absorption of radiolabeled peptides reduces the sensitivity for detection in the kidney's proximity for imaging purposes. The highest acceptable activity levels that can be given for therapeutic purposes without causing radiation nephrotoxicity are restricted by the renal accumulation of radiolabeled peptides. The kidneys are the organs that are dose-limited in the majority of peptide receptor radionuclide treatment (PRRT) cases.

In this study, there were 2 groups, each consisting of 4 mices; the first group was only injected with the tracer [^{18}F]ALF-3p-*C*-NETA-TATE (< 1 MBq) intravenous (i.v), and the second group 5 minutes before the tracer injection, injected intraperitoneal (i.p) gelofusine (40 mg), after 1 hour, animals were sacrificed and organs were counted. Values are presented as mean ± SD, and analysis was performed ANOVA with the significance level was set at $P < 0.01$.

4.3 Results and Discussion

4.3.1 Radiolabeling of 3p-C-NETA-TATE and DOTA-TATE

In the clinic, ^{177}Lu is the radiometal that is most frequently utilized for vectorized radionuclide therapy, and DOTA chelators are typically used to create theranostic pairs (for example, [^{177}Lu]Lu-DOTATATE used for therapy and [^{68}Ga]Ga-DOTATATE) applied for diagnostic purposes. Despite the excellent clinical results that DOTA has achieved with ^{177}Lu, the slow labeling kinetics which include labeling at high temperatures (for example, 95 °C), high ligand concentrations (for instance, 100 µM),

and long reaction times (30–60 min) are significant and are the main focus of chelator development.

According to iTLC results, [^{177}Lu]LuCl$_3$ was complexed by 3p-*C*-NETA in 12 min at 40 °C (RCC of 96.5± 0.7%), and compared with DOTA-TATE at the same condition (74.65 ± 1.8). These findings indicate the superior qualities of 3p-C-NETA as a chelator for ^{177}Lu.

Table 4.1. Radiolabeling [^{177}Lu]Lu-DOTA-TATE

Conc (µM)	40 °C	SD	60 °C	SD	95 °C	SD
0.1	17.7	1.2	28.49	0.8	31.4	1.4
0.5	28.73	1.5	33.53	0.7	62.1	1.3
1.0	36.61	2.3	44.42	1.4	73.3	0.4
5.0	41.59	0.9	61.54	1.7	82.6	0.7
10	74.65	1.8	92.7	1.9	99.4	0.9
20	96.13	2.4	98.79	1.1	99.6	1.6

Table 4.2. Radiolabeling [^{177}Lu]Lu-3p-*C*-NETA-TATE

Conc (µM)	40 °C	SD	60 °C	SD	95 °C	SD
0.1	38.6	1.0	42.3	1.3	51.2	1.3
0.5	69.7	1.6	78.9	1.4	81.3	1.2
1.0	74.6	1.3	82.3	1.7	89.4	1.4
5.0	88.4	0.9	90.5	1.5	92.3	1.3
10	96.5	0.7	99.1	1.6	99.2	1.2
20	98.7	1.6	99.6	1.2	99.5	0.7
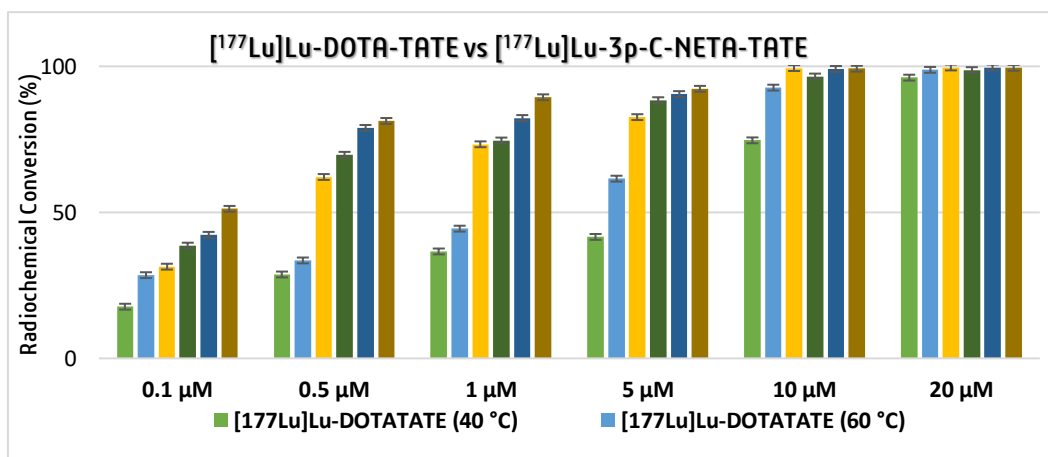
Figure 4.1. Radiolabeling of [^{177}Lu]Lu-DOTA-TATE vs [^{177}Lu]Lu-3p-*C*-NETA-TATE

According to iTLC results, [177Lu]LuCl$_3$ was complexed by 3p-C-NETA in 12 min at 40 °C (RCC of 96.5± 0.7%), and compared with DOTA-TATE at the same condition (74.65 ± 1.8). The 3p-C-NETA chelator can form a complex with radiometal ^{177}Lu at 40 °C with a better RCC compared to the complex with the DOTA chelator which is formed at 95°C, this is an advantage of the 3p-C-NETA chelator. These findings indicate the superior qualities of 3p-C-NETA as a chelator for [177]Lu.

4.3.2 *In vitro* stability of 3p-*C*-NETA-TATE and DOTA-TATE

The [177]Lu-3p-*C*-NETA-TATE in PBS and human serum at 3 days confirmed an intact radiocomplex of above 90 %, as anticipated and previously reported, at >95%. Nevertheless, it fell below 90 % after 5 days. This contrasts with ^{177}Lu-DOTA-TATE, which even after 7 days still maintains an intact radiocomplex above 95 %.
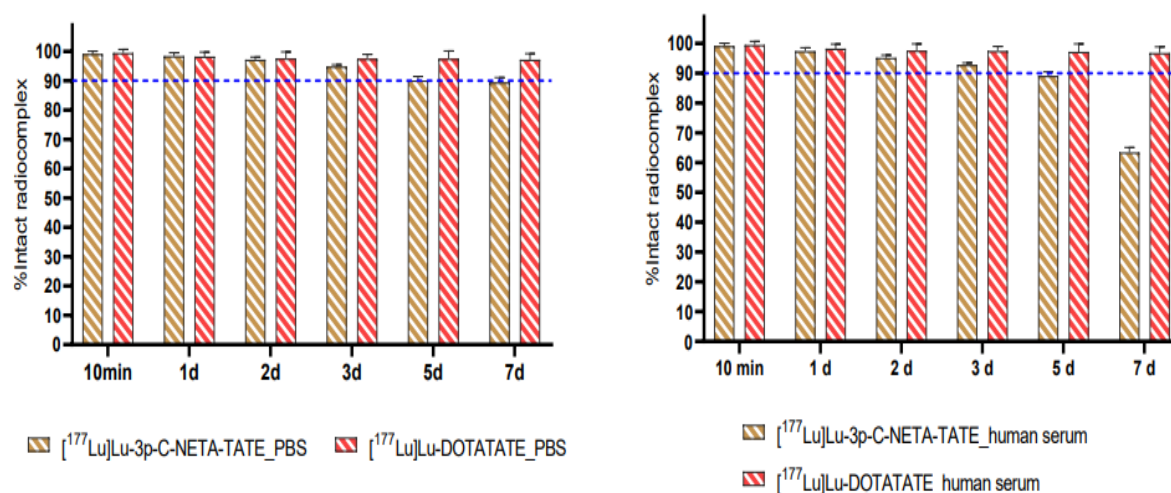
Figure 4.2. *In vitro* stability of[177Lu]Lu-DOTA-TATE vs [177Lu]Lu-3p-*C*-NETA-TATE in PBS and HS

4.3.3 Cell Binding and Internalization Studies

Incubation of [177Lu]Lu-3p-*C*-NETA-TATE with BON1-SSTR2 cells revealed selective binding to SSTR2, which was significantly blocked by the addition of an excess of unlabeled octreotide acetate (100 µM) (figure 7). It has relatively the same binding pattern compared to [177Lu]Lu-DOTA-TATE.
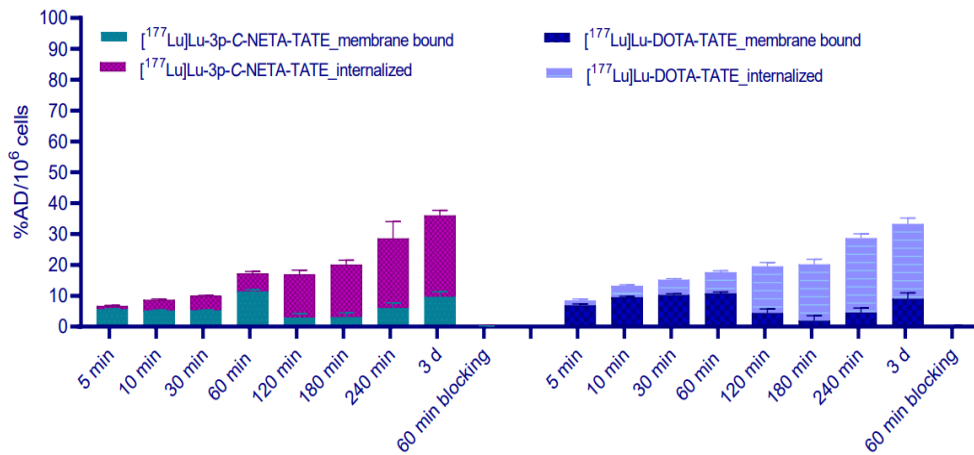
Figure 4.3. *In vitro* assays using BON1-SSTR2 confirmed the receptor-mediated tumor cell targeting of [^{177}Lu]Lu-3p-*C*-NETA-TATE and [^{177}Lu]Lu-DOTA-TATE

4.3.4 Cell Viability Test

The cytotoxic effect was used to determine the ability of [^{177}Lu]Lu-3p-*C*-NETA-TATE to kill antigen-specific BON-1 tumor cells. Observations were made with 22 dose activity series from the lowest 3 KBq, up to 150 MBq (figure 5). The capacity of BON-1 cells to repopulate was lower upon the addition of higher concentrations of [^{177}Lu]Lu-*C*-NETA-TATE, this observation condition was not much different compared to [^{177}Lu]Lu-DOTA-TATE.
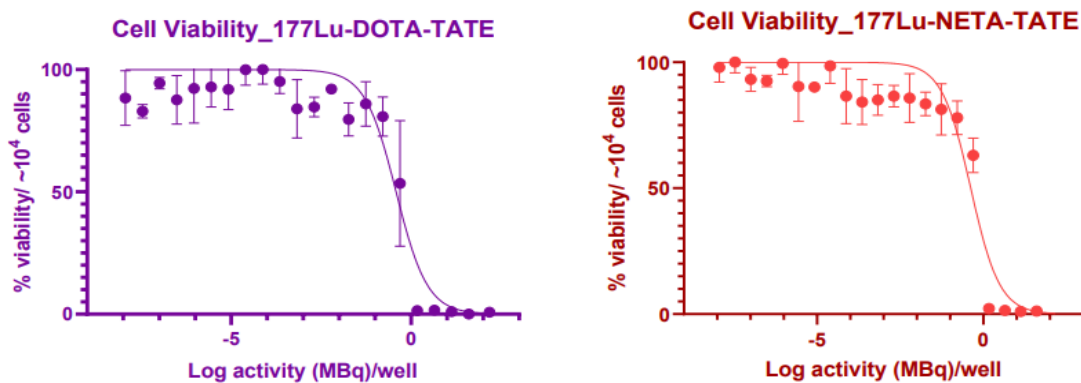
Figure 4.4. [^{177}Lu]Lu-3p-*C*-NETA-TATE and [^{177}Lu]Lu-DOTA-TATE inhibit BON1-SSTR2 cell growth *in vitro*

43

4.3.5 Clonogenic Assay

Assessment of the clonogenic ability of BON1 cells after exposure to an increasing radioactive amount (0-1.7 MBq] of [^{177}Lu]Lu-3p-*C*-NETA-TATE and [^{177}Lu]Lu-DOTA-TATE (figure 4) revealed a dose-dependent decrease in colony-forming cells. The addition of 0.1 Mbq resulted in 48 % of the reference amount of colonies (non-radioactive control), which further decreased to 20% after addition of 1.7 Mbq.
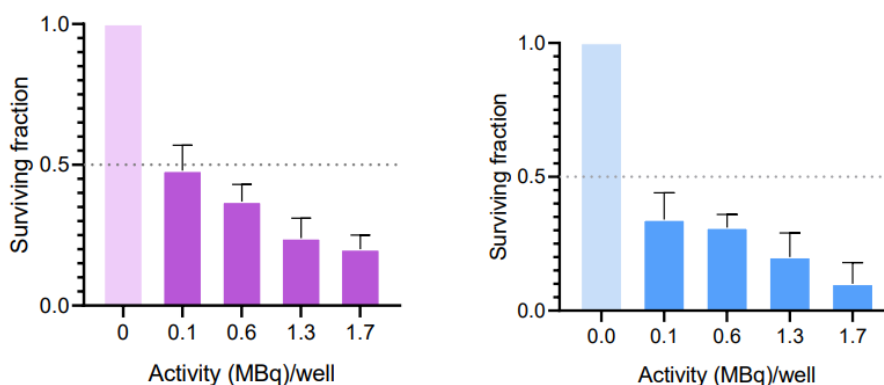
Figure 4.5. The determined colony area percentages performed a dose-response correlation analysis of [^{177}Lu]Lu-3p-*C*-NETA-TATE and [^{177}Lu]Lu-DOTA-TATE

4.3.6 *In vivo* biodistribution of 3p-*C*-NETA-TATE

These studies have indicated that the coadministration of basic compounds of low doses of polygelines (e.g., gelofusine [Braun]) significantly reduces the radioactivity concentrations in the kidneys. The biodistribution of [^{18}F]AlF-3p-*C*-NETA-TATE is shown in Figure 4.6. We also demonstrated that the administration of gelofusine (40 mg) efficiently reduced the kidney uptake of [^{18}F]AlF-3p-*C*-NETA-TATE in mices.

Many studies have been performed to investigate the mechanism of renal absorption of this radiolabeled peptide. The proximal tubular cells are thought to take up the process, partially through fluid-phase endocytosis and partially through receptor-mediated endocytosis, where the megalin and cubilin receptors are thought to play a significant role. The receptor has several binding domains, binds a wide range of proteins and peptides, and is important for the reabsorption of a large number of proteins and peptides that have been filtered. Megalin has been shown in multiple studies to bind to

cationic drugs and proteins that are rich in positively charged amino acids. Receptor-mediated endocytosis of radiolabeled peptides is predicted to be blocked by these cationic amino acids through their interaction with negatively charged receptor sites.
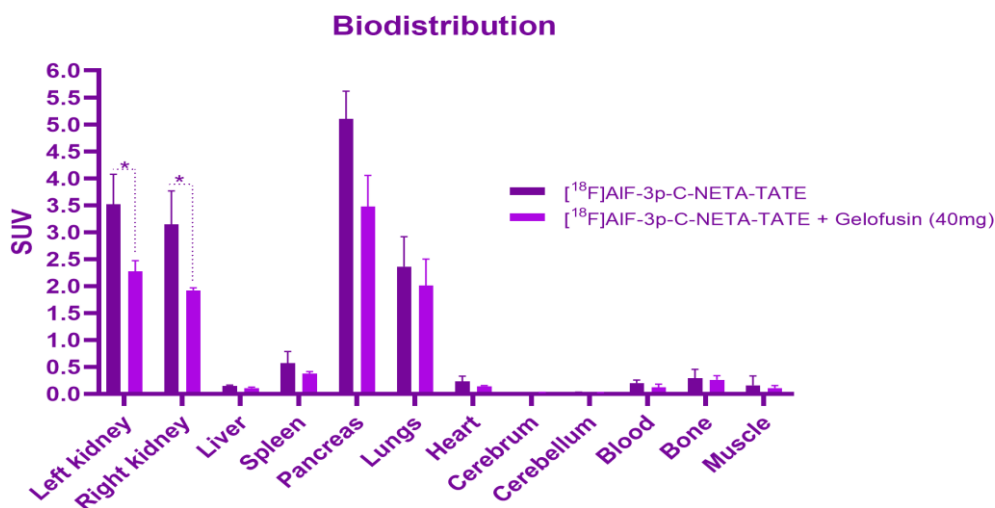
Figure 4.6. Biodistribution of [^{18}F]AlF-3p-C-NETA-TATE

The present study demonstrates that the kidney uptake of [^{18}F]AlF-3p-C-NETA-TATE was significantly decreased by the gelatin-based plasma expander gelofusine. Gelofusine is used for reducing a patient's kidney's absorption of radiolabeled peptides, it is recommended to administer the radiolabel almost immediately following the injection of gelofusine. Gelofusine's effect on people is likely to persist longer than fifteen minutes because humans eliminate it more slowly than tiny animals do. Gelofusine administration is safe. Gelofusine administration does not cause adverse effects, even at high dosages.

4.4 Conclusion

For the first time, the 3p-C-NETA-TATE precursor's evaluation and characterization against BON1-SSTR2 cells are reported in this study, compared to DOTA-TATE as a benchmark. The radiolabeling evaluation provides information that labeling 3p-C-NETA-TATE with ^{177}Lu gives very promising results, where labeling can be done in 12 min at 40 °C (RCC of 96.5 ± 0.7%), and different results when compared with DOTA-TATE under the same conditions (74.65 ± 1.8). This is why 3p-C-NETA is an ideal chelator for ^{177}Lu, as it can be utilized for labeling any type of heat-sensitive

biomolecule in these mild conditions. In addition, the *in vitro* evaluation showed that the 3p-*C*-NETA-TATE precursor had similar characteristics to DOTA-TATE. This makes 3p-*C*-NETA-TATE very potential for therapeutic purposes and diagnosis of NETs.

Chapter 5

Conclusion and future directions

5.1 Conclusion

In this thesis, I performed DFT calculations to obtain the formation constant of the radiometal-chelator complex by evaluating the formation constant and conceptual DFT-Based Properties. The DFT results show that the 3p-*C*-NETA chelator is very promising as a ^{177}Lu $^{3+}$ chelator, as well as a ^{213}Bi radiometal emitter for aplha therapy. The DFT calculation results show results that are in line with the in vitro evaluation. Meanwhile, the chelator for ^{225}Ac $^{3+}$ is 3p-C-DEPA. I also managed to evaluate the *in vitro* characterization of the 3p-C-NETA-TATE precursor labeled ^{177}Lu, with DOTA-TATE as a benchmark. The similarity of the results of 3p-C-NETA-TATE with DOTA-TATE showed promise as a chelator for NETs therapy. In addition, another study also reported that 3p-C-NETA-TATE labeled with Al^{18}F showed good results in radiochemical conversion and stability *in vitro*. So it can be concluded that the 3p-*C*-NETA-TATE precursor can be a theranostic precursor for NETs.

5.2 Future directions

As discussed in section 4.1, the development of chelator and precursor alpha therapy such as ^{225}Ac and ^{213}Bi is a promising solution to overcome [^{177}Lu]Lu-DOTA-TATE treatment which was reported in decades where there were several cases of relapse after several years of first stage treatment. Therefore, it is necessary to carry out tests to evaluate the relative biological effectiveness (RBE) between the two radioisotopes alpha particle and beta particle. DNA double-strand breaks (DSB) testing can evaluate the effectiveness of using these radioisotopes.

In vitro and *in vivo* radiocomplex evaluation of alpha particle [^{213}Bi]-Bi-3p-C-NETA-TATE, and [^{225}Ac]Ac-DEPA-TATE compared to [^{177}Lu]Lu-3p-C-NETA-TATE will show success of alpha particle therapy for NETs. This data will be the underlying data for testing the next stage of clinical trials.

Bibliography

1. Aohan Nu, Victoria B, Samantha NM, Valery R, Hua Y, et.al, Chelating the Alpha Therapy Radionuclides ^{225}Ac^{3+} and ^{213}Bi^{3+} with 18-Membered Macrocyclic Ligands Macrodipa and Py-Macrodipa, Inorg Chem. 2022 January 17; 61(2): 801–806

2. Bolzati, C.; Refosco, F.; Marchiani, A.; Ruzza, P. Curr. Med. Chem. 2010, 17, 2656–2683

3. Cherry, S., Sorenson, J., Phelps, M., 2012. Physics in Nuclear Medicine. Saunders, Philadelphia.

4. Madsen, M.T., 2007. Recent advances in SPECT imaging. J. Nucl. 48, 661–673.

5. Verel, I.; Visser, G. W. M.; van Dongen, G. A. J. Nucl. Med. 2005, 46 Suppl 1, 164S – 171S.

6. Wadas, T. J.; Wong, E. H.; Weisman, G. R.; Anderson, C. J. Chem. Rev. 2010, 110, 2858– 2902.

7. Zeglis, B. M.; Lewis, J. S. Dalton Trans. 2011, 40, 6168–6195

8. Rahmim, A., Zaidi, H., 2008. PET versus SPECT: strengths, limitations and challenges. Nucl. Med. Commun. 29 (3), 193–207.

9. Volkert, W. A.; Goeckeler, W. F.; Ehrhardt, G. J.; Ketring, A. R. J. Nucl. Med. 1991, 32, 174– 185.

10. Kramer-Marek, G.; Capala, J. The role of nuclear medicine in modern therapy of cancer. Tumor Biol. 2012, 33, 629–640.

11. Kumar, C.; Shetake, N.; Desai, S.; Kumar, A.; Samuel, G.; Pandey, B.N. Relevance of radiobiological concepts in radionuclide therapy of cancer. Int. J. Radiat. Biol. 2016, 92, 173–186.

12. Qaim, S.M. Therapeutic radionuclides and nuclear data. Radiochim. Acta 2001, 89, 297–304.

13. Baskar, R.; Dai, J.; Wenlong, N.; Yeo, R.; Yeoh, K.W. Biological response of cancer cells to radiation treatment. Front. Mol. Biosci. 2014, 1, 24.

14. Herrmann, K.; Schwaiger, M.; Lewis, J.S.; Solomon, S.B.; McNeil, B.J.; Baumann, M.; Gambhir, S.S.; Hricak, H.; Weissleder, R. Radiotheranostics: A roadmap for future development. Lancet Oncol. 2020, 21, e146–e156.

15. Pouget, J.P.; Navarro-Teulon, I.; Bardiès, M.; Chouin, N.; Cartron, G.; Pèlegrin, A.; Azria, D. Clinical Radioimmunotherapy—The role of radiobiology. Nat. Rev. Clin. Oncol. 2011, 8, 720–734.

16. Persson, L. The Auger electron effect in radiation dosimetry. Health Phys. 1994, 67, 471–476.

17. Sgouros, G.; Bodei, L.; McDevitt, M.R.; Nedrow, J.R. Radiopharmaceutical therapy in cancer: Clinical advances and challenges. Nat. Rev. Drug Discov. 2020, 19, 589–608.

18. Navalkissoor, S.; Grossman, A. Targeted alpha particle therapy for neuroendocrine tumours: The next generation of peptide receptor radionuclide therapy. Neuroendocrinology 2019, 108, 256–264.

19. Yeong, C.H.; Cheng, M.H.; Ng, K.H. Therapeutic Radionuclides in Nuclear Medicine: Current and Future Prospects. J. Zhejiang Univ. Sci. B 2014, 15, 845–863.

20. Ferrier, M.G.; Radchenko, V. An appendix of radionuclides used in targeted alpha therapy. J. Med. Imaging Radiat. Sci. 2019, 50, S58–S65.

21. Guerra Liberal, F.D.C.; O'Sullivan, J.M.; McMahon, S.J.; Prise, K.M. Targeted Alpha Therapy: Current Clinical Applications. Cancer Biother. Radiopharm. 2020, 35, 404–417.

22. Ahenkorah, S.; Cassells, I.; Deroose, C.; Cardinaels, T.; Burgoyne, A.; Bormans, G.; Ooms, M.; Cleeren, F. Bismuth-213 for Targeted Radionuclide Therapy: From Atom to Bedside. Pharmaceutics 2021, 3, 599.

23. Miller, P. W.; Long, N. J.; Vilar, R.; Gee, A. D. Angew. Chem. Int. Ed. Engl. 2008, 47, 8998– 9033.

24. Bhattacharyya, S.; Dixit, M. Dalton Trans. 2011, 40, 6112–6128.

25. Wadas, T. J.; Wong, E. H.; Weisman, G. R.; Anderson, C. J. Chem. Rev. 2010, 110, 2858– 2902.

26. Clinical Trials. http://www.clinicaltrials.gov/ (accessed June 2023).

27. Hassfjell, S.; Brechbiel, M. W. Chem. Rev. 2001, 101, 2019–2036.

28. Bartholomä, M. D. Inorganica Chim. Acta 2012, 389, 36–51.

29. Deri, M. A.; Zeglis, B. M.; Francesconi, L. C.; Lewis, J. S. Nucl. Med. Biol. 2013, 40, 3–14.

30. Chang, A. J.; Silva, R. A. De; Lapi, S. E. Mol. Imaging 2013, 12, 17–27.

31. Ferreiros-Martinez, R.; Esteban-Gomez, D.; Platas-Iglesias, C.; de Blas, A.; Rodriguez-Blas, T. Dalton Trans. 2008, 42, 5754–5765.

32. Ferreirós-Martínez, R.; Esteban-Gómez, D.; Platas-Iglesias, C.; De Blas, A.; Rodríguez-Blas, T. Inorg. Chem. 2009, 48, 10976–10987.

33. Boros, E.; Ferreira, C. L.; Cawthray, J. F.; Price, E. W.; Patrick, B. O.; Wester, D. W.; Adam, M. J.; Orvig, C. J. Am. Chem. Soc. 2010, 132, 15726–15733.

34. Correia, J. D. G.; Paulo, A.; Raposinho, P. D.; Santos, I. Dalt. Trans. 2011, 40, 6144–6167.

35. Craig, A. S.; Parker, D.; Adams, H.; Bailey, N. A. J. Chem. Soc., Chem. Commun. 1989, 1, 1793–1794.

36. Strosberg J, El-Haddad G, Wolin E, Hendifar A, Yao J, Chasen B, et al. NETTER-1 Trial Investigators. Phase 3 trial of 177Lu-DOTATATE for midgut neuroendocrine tumours. N Engl J Med. 2017;376:125–35.

37. Kim SJ, Pak K, Koo PJ, Kwak JJ, Chang. The efficacy of 177Lu-labelled peptide receptor radionuclide therapy in patients with Eur J Nucl Med Mol Imaging (2020) 47:934–946 945 neuroendocrine tumours: a meta-analysis. Eur J Nucl Med Mol Imaging. 2015;42:1964–70.

38. Rösch, F.; Baum, R. Dalton Trans. 2011, 40, 6104–6111.

39. Riesen, A.; Kaden, T. A.; Ritter, W.; Maecke, H. R. J. Chem. Soc. Chem. Commun. 1989, 460– 462

40. Sun, H.; Cox, M. C.; Li, H.; Sadler, P. J. Sruct. Bond. 1997, 88, 72–102.

41. Yong, K.; Brechbiel, M. W. Dalton Trans. 2011, 40, 6068–6076.

42. Chappell, L. L.; Dadachova, E.; Milenic, D. E.; Garmestani, K.; Wu, C.; Brechbiel, M. W. Nucl. Med. Biol. 2000, 27, 93–100.

43. Clinical Trials. http://www.clinicaltrials.gov/ (accessed June 2023)

44. Notni, J.; Hermann, P.; Havlícková, J.; Kotek, J.; Kubíček, V.; Plutnar, J.; Loktionova, N.; Riss, P. J.; Rösch, F.; Lukeš, I. Chem. A Eur. J. 2010, 16, 7174–7185.

45. Notni, J.; Šimeček, J.; Hermann, P.; Wester, H.-J. Chem. A Eur. J. 2011, 17, 14718–14722

46. Shokeen, M.; Wadas, T. J. Med. Chem. 2011, 7, 413–429.

47. Bartholomä, M. D. Inorganica Chim. Acta 2012, 389, 36–51.

48. Shokeen, M.; Wadas, T. J. Med. Chem. 2011, 7, 413–429.

49. Bartholomä, M. D. Inorganica Chim. Acta 2012, 389, 36–51.

50. Chappell, L. L.; Deal, K. A.; Dadachova, E.; Brechbiel, M. W. Bioconjugate Chem. 2000, 11, 510–519.

51. Stephen A, Erika M, Christopher C, Christophe MD, Guy B, Fredererik C, et. Al. 3p-C-NETA: A versatile and effective chelator for development of Al^{18}F-labeled and therapeutic radiopharmaceuticals. Theranostics. 2022; 12(13): 5971-5985.

52. Chong HS, Song HA, Kang CS, Sun X, Jia F, Song HA, Chen Y, et.al, A highly effective bifunctional ligand for radioimmunotherapy applications, Chem. Commun., 2011, 47, 5584–5586

53. Chong HS, Sun X, Chen Y, Sin Y, Kang CS, et.al, Synthesis and comparative biological evaluation of bifunctional ligands for radiotherapy applications of ^{90}Y and ^{177}Lu, Bioorg. Med. Chem. 23 (2015) 1169–1178

54. Jones, R.O. Density functional theory: Its origins, rise to prominence, and future. Rev. Mod. Phys. 2015, 87, 897–923.

55. Janesko, B.G. Replacing hybrid density functional theory: Motivation and recent advances. Chem. Soc. Rev. 2021, 50, 8470–8495.

56. El-Nahas, A.M.; Simmie, J.; Mangood, A.H.; Hirao, K.; Song, J.-W.; Watson, M.A.; Taketsugu, T.; Koga, N. Assessment of hybrid, meta-hybrid-GGA, and long-range corrected density functionals for the estimation of enthalpies of formation, barrier heights, and ionisation potentials of selected C1–C5 oxygenates. Mol. Phys. 2015, 113, 1630–1635.

57. Harper, L.K.; Shoaf, A.L.; Bayse, C.A. Predicting trigger bonds in explosive materials through Wiberg bond index analysis. Phys. Chem. Chem. Phys. 2015, 16, 3886–3892.

58. Jeong, K.; Sung, I.; Joo, H.U.; Kwon, T.; Yuk, J.M.; Kwon, Y.; Kim, H. Molecular design of nitro-oxide-substituted cycloalkane derivatives for high-energy-density materials. J. Mol. Struct. 2020, 1212, 128128.

59. Chaves, A.S.; Piotrowski, M.J.; Da Silva, J.L.F. Evolution of the structural, energetic, and electronic properties of the 3d, 4d, and 5d transition-metal clusters (30 TMn systems for n = 2–15): A density functional theory investigation. Phys. Chem. Chem. Phys. 2017, 19, 15484–15502.

60. O'Connor, N.J.; Jonayat, A.S.M.; Janik, M.J.; Senftle, T.P. Interaction trends between single metal atoms and oxide supports identified with density functional theory and statistical learning. Nat. Catal. 2018, 1, 531–539.

61. Narendrapurapu, B.S.; Richardson, N.A.; Copan, A.V.; Estep, M.L.; Yang, Z.; Schaefer, I.H.F. Investigating the effects of basis set on metal–metal and metal–ligand bond distances in stable transition metal carbonyls: Performance of correlation consistent basis sets with 35 density functionals. J. Chem. Theory Comput. 2013, 9, 2930–2938.

62. Cross, J.N.; Su, J.; Batista, E.R.; Cary, S.K.; Evans, W.J.; Kozimor, S.A.; Mocko, V.; Scott, B.L.; Stein, B.W.; Windorff, C.J.; et al. Covalency in americium(III) hexachloride. J. Am. Chem. Soc. 2017, 139, 8667–8677.

63. Gutten, O.; Rulísek, L. Predicting the Formation constants of˘ Metal-Ion Complexes from First Principles. Inorg. Chem. 2013, 52 (18), 10347−10355.

64. Brechbiel MW Targeted α-Therapy: Past, Present, Future? Dalton Trans. 2007, 4918–4928.

65. Seidl C, Radioimmunotherapy with α-Particle-Emitting Radionuclides. Immunotherapy 2014, 6, 431–458.

66. Guerra Liberal FDC; O'Sullivan JM; McMahon SJ; Prise KM Targeted Alpha Therapy: Current Clinical Applications. Cancer Biother. Radiopharm 2020, 35, 404–417.

67. Yang H; Wilson JJ; Orvig C; Li Y; Wilbur DS; Ramogida C; Radchenko V; Schaffer P Harnessing Alpha-Emitting Radionuclides for Therapy: Radiolabeling Method Review. J. Nucl. Med 2021.

68. Sanjana B, Madhav PY, Chandrasekhar B, Ranjit KS, Madhavi T, Broadening horions with ^{225}Ac-DOTATATE targeted alpha therapy for gastroenteropancreatic neuroendocrine tumour patients stable or refractory to ^{177}Lu-DOTATATE PRRT: first clinical experience on the efficacy and safety. European Journal of Nuclear Medicine and Molecular Imaging (2020) 47:934–946.

69. Geerlings MW; Kaspersen FM; Apostolidis C; van der Hout R The Feasibility of 225Ac as a Source of α-Particles in Radioimmunotherapy. Nucl. Med. Commun 1993, 14, 121–125.

70. Morgenstern A; Apostolidis C; Kratochwil C; Sathekge M; Krolicki L; Bruchertseifer F An Overview of Targeted Alpha Therapy with 225Actinium and 213Bismuth. Curr. Radiopharm 2018, 11, 200–208.

71. Kratochwil C, Bruchertseifer F, Giesel FL, Weis M, Verburg FA, Mottaghy F, et al. ^{225}Ac-PSMA-617 for PSMA-targeted α-radiation therapy of metastatic castration-resistant prostate Cancer. J Nucl Med. 2016;57:1941–4.

72. Morgenstern A; Bruchertseifer F; Apostolidis C Bismuth-213 and Actinium-225 – Generator Performance and Evolving Therapeutic Applications of Two Generator-Derived Alpha-Emitting Radioisotopes. Curr. Radiopharm 2012, 5, 221–227.

73. Ahenkorah S; Cassells I; Deroose CM; Cardinaels T; Burgoyne AR; Bormans G; Ooms M; Cleeren F Bismuth-213 for Targeted Radionuclide Therapy: From Atom to Bedside. Pharmaceutics 2021, 13, 599.

74. Hassfjell S; Brechbiel MW The Development of the α-Particle Emitting Radionuclides ^{212}Bi and ^{213}Bi, and Their Decay Chain Related Radionuclides, for Therapeutic Applications. Chem. Rev 2001, 101, 2019–2036.

75. Brechbiel, M. W. Q. J. Nucl. Med. Mol. Imaging 2008, 52, 166.

76. Nikula, T. K., McDevitt, M. R., Finn, R. D., Wu, C., Kozak, R. W., Garmasteni,et.al, (1999) Alpha-emitting bismuth cyclohexylbenzyl DTPA

constructs of recombinant humanized anti-CD33 antibodies: Pharmacokinetics, bioactivity, toxicity, and chemistry. J. Nucl. Med. 40, 166–76.

77. Kim Y-S; Brechbiel MW, An Overview of Targeted Alpha Therapy. Tumor Biol. 2012, 33, 573– 590.

78. Stephen A, Erika M, Christopher C, Christophe MD, Guy B, Fredererik C, et. Al. 3p-C-NETA: A versatile and effective chelator for development of Al^{18}F-labeled and therapeutic radiopharmaceuticals. Theranostics. 2022; 12(13): 5971-5985.

79. Deal KA, Davis IA, Mirzadeh S, et al. Improved in vivo stability of actinium-225 macrocyclic complexes. J Med Chem 1999;42:2988.

80. Aohan Nu, Victoria B, Samantha NM, Valery R, Hua Y, et.al, Chelating the Alpha Therapy Radionuclides ^{225}Ac^{3+} and ^{213}Bi^{3+} with 18-Membered Macrocyclic Ligands Macrodipa and Py-Macrodipa, Inorg Chem. 2022 January 17; 61(2): 801– 806.

81. Cassells I, Ahenkorah S, Burgoyne AR, Van de Voorde M, Deroose CM, Cardinaels T, et al. Radiolabeling of Human Serum Albumin With Terbium-161 Using Mild Conditions and Evaluation of in vivo Stability. Front Med (Lausanne), 2021; 8: 675122.

82. M. Edouard, P. Romain, S. Baptiste, N.J. Jean, Estimation of solvation quantities from experimental thermodynamic data: development of the comprehensive compsol databank for pure and mixed solutes, J. Phys. Chem. Ref. Data 46 (2017) 1–22.

83. Danni Ramdhani, Hiroshi Watabe, Eva Maria Widyasari, Maula eka Sriyani, Quizheilla Putri Arnada. Heliyon. 2020 Sep; 6(9): e04780.

84. R.G. Pearson, Chemical Hardness: Applications from Molecules to Solids (Wiley-VCH, Weinheim, 1997).

85. McDevitt MR, Ma D, Simon J, Frank RK, Scheinberg DA. Design and synthesis of ^{225}Ac radioimmunopharmaceuticals. Appl Radiat Isot. 2002;57(6):841–7.

86. Eychenne R, Chérel M, Haddad F, Guérard F, Gestin JF. Overview of the Most Promising Radionuclides for Targeted Alpha Therapy: The "Hopeful Eight." Pharmaceutics. 2021;13(6).

87.   Ramogida CF, Robertson AKH, Jermilova U, Zhang C, Yang H, Kunz P, et al. Evaluation of polydentate picolinic acid chelating ligands and an α-melanocyte-stimulating hormone derivative for targeted alpha therapy using ISOL-produced 225Ac. EJNMMI radiopharm chem. 2019;4(1):1–20.

88.   Song HA, Kang CS, Baidoo KE, Milenic DE, Chen Y, Dai A, et al. Efficient Bifunctional Decadentate Ligand 3p-C-DEPA for Targeted α-Radioimmunotherapy Applications. Bioconjug Chem. 2011 Jun 15;22(6):1128–35.

89.   Garmestani K, Yao Z, Zhang M, Wong K, Park CW, Pastan I, et al. Synthesis and evaluation of a macrocyclic bifunctional chelating agent for use with bismuth radionuclides. Nucl Med Biol. 2001;28(4): 409–18.

90.   Y. Gao, P. Grover, G. Schreckenbach, Stabilization of hydrated AcIII cation: the role of superatom states in actinium-water bonding, Chem. Sci. 2021, 12(7), 2655.

91.   S.A. Cotton, Paul RR, A. Shield, JM Harrowfield, A comparison of the structural chemistry of scandium, yttrium, lanthanum and lutetium: A contribution to the group 3 debate, Coordination Chemistry Reviews 455 (2022) 214366.

92.   M. Ale Brown, Thomas B, David, AR, Examination of lutetium(III)-DOTA and copper(II)-NOTA solution structures using EXAFS, Inorganica Chimica Acta 482 (2018) 118–121.

93.   Z. Yan, G.T. Donald, The M06 suite of density functionals for main group thermochemistry, thermochemical kinetics, noncovalent interactions, excited states, and transition elements: two new functionals and systematic testing of four M06-class functionals and 12 other functionals, Theoret. Chemistry Accounts 120 (2008) 215–241.

94.   Chen H, Shi R, Ow H, Predicting Formation constants for Terbium(III) Complexes with Dipicolinic Acid and 4-Substituted Dipicolinic Acid Analogues using Density Functional Theory, ACS Omega 2019, 4, 20665-20671.

95.   Rinke A, Müller HH, Schade-Brittinger C, Klose KJ, Barth P, Wied M, et al. PROMID Study Group. A placebo-controlled, doubleblind, prospective, randomized study on the effect of octreotide LAR in the control of tumour growth

in patients with metastatic neuroendocrine midgut tumours: a report from the PROMID Study Group. J Clin Oncol 2009;7:4656–4663.

96. Delavault P, Caplin ME, Liyanage N, Blumberg J. The CLARINET study: assessing the effect of lanreotide autogel on tumour progression-free survival in patients with nonfunctioning gastroenteropancreatic neuroendocrine tumours. J Clin Oncol. 2017;30(15_suppl).

97. Yao JC, Fazio N, Singh S, Buzzoni R, Carnaghi C, Wolin E, et al. RAD001 in Advanced Neuroendocrine Tumours, Fourth Trial (RADIANT-4) Study Group. Everolimus for the treatment of advanced, non-functional neuroendocrine tumours of the lung or gastrointestinal tract (RADIANT-4): a randomised, placebo-controlled, phase 3 study. Lancet. 2016;387:968–77.

98. Raymond E, Dahan L, Raoul JL, Bang YJ, Borbath I, Lombard Bohas C, et al. Sunitinib malate for the treatment of pancreatic neuroendocrine tumours. N Engl J Med. 2011;364:501–13.

99. Yao JC. Neuroendocrine tumours. molecular targeted therapy for carcinoid and islet-cell carcinoma. Best Pract Res Clin Endocrinol Metab. 2017;21:163–72.

100. Strosberg J, El-Haddad G, Wolin E, Hendifar A, Yao J, Chasen B, et al. NETTER-1 Trial Investigators. Phase 3 trial of ^{177}Lu-DOTATATE for midgut neuroendocrine tumours. N Engl J Med. 2017;376:125–35.

101. Kim SJ, Pak K, Koo PJ, Kwak JJ, Chang. The efficacy of ^{177}Lu-labelled peptide receptor radionuclide therapy in patients neuroendocrine tumours: a meta-analysis. Eur J Nucl Med Mol Imaging. 2015;42:1964–7.

102. Tworowska I, Ranganathan D, Thamake S, Delpassand E, Mojtahedi A, Schultz MK, et al. Radiosynthesis of clinical doses of ^{68}Ga-DOTATATE (GalioMedixTM) and validation of organic-matrix-based [68]Ge/^{68}Ga generators. Nucl Med Biol. 2016; 43(1): 19–26.

103. Pauwels E, Cleeren F, Bormans G, Deroose CM. Somatostatin receptor PET ligands - the next generation for clinical practice. Am J Nucl Med Mol Imaging. 2018; 8(5): 311.Imaging. 2018; 8(5): 311.

104. Vermeulen K, Vandamme M, Bormans G, Cleeren F. Design and Challenges of Radiopharmaceuticals. Semin Nucl Med. 2019; 49(5): 339–56.

105. Rodnick ME, Sollert C, Stark D, Clark M, Katsifis A, Hockley BG, et al. Cyclotron-based production of ^{68}Ga, [^{68}Ga]GaCl3, and [^{68}Ga]Ga-PSMA-11 from a liquid target. EJNMMI Radiopharm Chem. 2020;5(1):1–18.

106. Giesel FL, Adeberg S, Syed M, Lindner T, Jiménez-Franco LD, Mavriopoulou E, et al. FAPI-74 PET/CT Using Either ^{18}F-AlF or Cold-Kit ^{68}Ga Labeling: Biodistribution, Radiation Dosimetry, and Tumor Delineation in Lung Cancer Patients. J Nucl Med. 2021;62(2):201–7.

107. Pauwels E, Cleeren F, Tshibangu T, Koole M, Serdons K, Dekervel J, et al. [^{18}F]AlF-NOTA-octreotide PET imaging: biodistribution, dosimetry and first comparison with [^{68}Ga]Ga-DOTATATE in neuroendocrine tumour patients. Eur J Nucl Med Mol Imaging. 2020;47(13):3033–46.

108. Altmann A, Haberkorn U, Siveke J. The Latest Developments in Imaging of Fibroblast Activation Protein. J Nucl Med. 2021;62(2):160–7.

109. Ahenkorah S, Cassells I, Deroose CM, Cardinaels T, Burgoyne AR, Bormans G, et al. Bismuth-213 for Targeted Radionuclide Therapy: From Atom to Bedside. Pharmaceutics. 2021;13(5):599.

110. Kang CS, Sun X, Jia F, Song HA, Chen Y, Lewis M, et al. Synthesis and preclinical evaluation of bifunctional ligands for improved chelation chemistry of ^{90}Y and ^{177}Lu for targeted radioimmunotherapy. Bioconjug Chem. 2012; 23(9):1775–82.

111. Kang CS, Song HA, Milenic DE, Baidoo KE, Brechbiel MW, Chong HS. Preclinical evaluation of NETA-based bifunctional ligand for radioimmunotherapy applications using ^{212}Bi and ^{213}Bi: Radiolabeling, serum stability, and biodistribution and tumor uptake studies. Nucl Med Biol. 2013; 40(5): 600–5.

112. Angus P. R. Johnston, Marloes M. J. Kamphuis, Georgina K. Such, Andrew M. Scott, Edouard C. Nice, Targeting Cancer Cells: Controlling the Binding and Internalization of Antibody-Functionalized Capsules, ACS nano, 2012, Vol. 6 , NO. 8 , 6667–6674.

113. Ishiyama M, Tominaga H, Shiga M, Sasamoto K, Okhura Y, Ueno KA. Combined assay of cell viability and in vitro cytotoxicity with a highly water-soluble

tetrazolium salt, neutral red and crystal violet. Biological & Pharmaceutical Bulletin. 1996;19(11):1518-1520

114. Sliwka L, Wiktorska K, Suchocki P, Milczarek M, et al. The comparison of MTT and CVS assays for the assessment of anticancer agent interactions. PLoS One. 2016;11(5):e0155722.

115. Nicolaas A P Franken, Hans M Rodermond, Jan Stap, Jaap Haveman, Chris van Bree, Clonogenic assay of cells *in vitro,* Nature Protocols, 2006, Vol.1, No.5

Appendix

A.   DFT optimized structure of complex

A.1 DFT optimized structure of Lu³⁺ complexes

[Lu(DOTA)(H₂O)]⁻   [Lu(3p-*C*-NETA)(H₂O)]⁻   [Lu(3p-*C*-DEPA)]²⁻
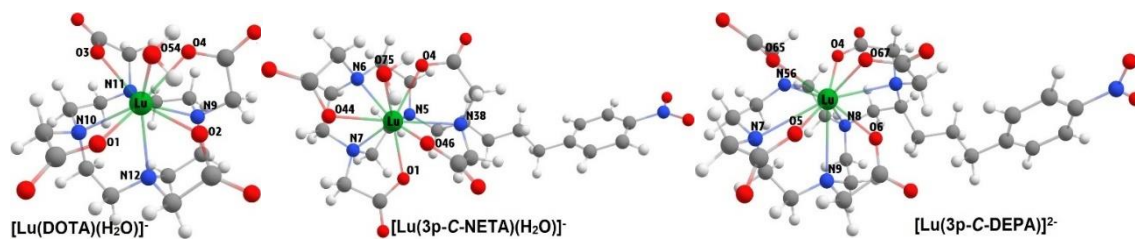
A.2 DFT optimized structure of Bi³⁺ complexes

[Bi(DOTA)(H₂O)]⁻   [Bi(3p-*C*-NETA)(H₂O)]⁻   [Bi(3p-*C*-DEPA)]²⁻
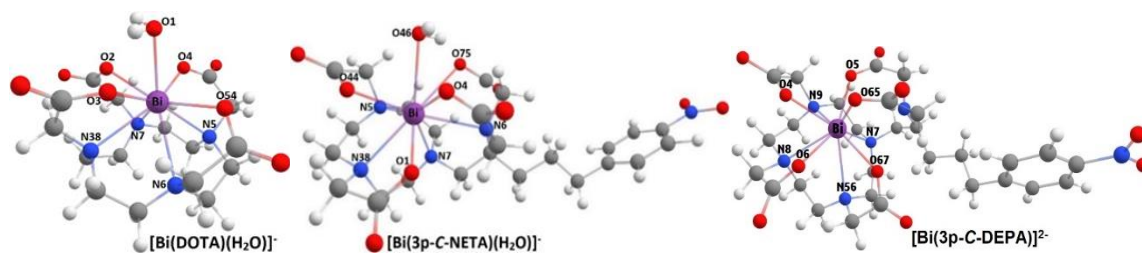
A.3 DFT optimized structure of Ac³⁺ complexes

[Ac(DOTA)(H₂O)]⁻   [Ac(3p-*C*-NETA)(H₂O)]⁻   [Ac(3p-*C*-DEPA)]²⁻
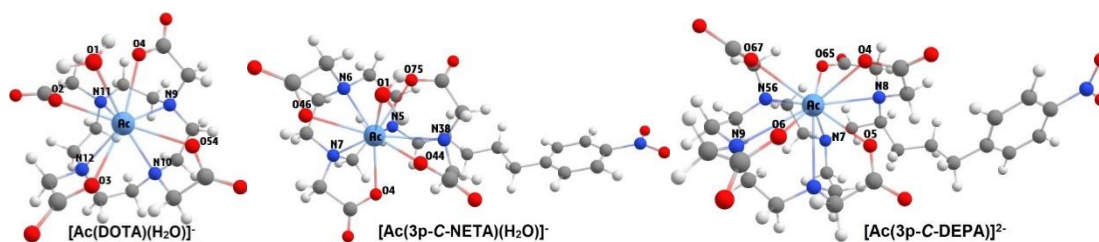
B. Cartesian coordinates of complex

B.1 Cartesian coordinates of Lu³⁺ complexes

Cartesian coordinates of the most important optimized structures (Angstroms).

Cartesian coordinate of [Lu(DOTA)(H₂O)]⁻complex

Atom	X	Y	Z
O	-2.05878	1.23606	-1.27348
O	1.34118	2.40801	-0.96505
O	-1.45468	-1.88311	-0.87494
O	2.13565	-1.4288	-1.31244
O	-4.24121	1.8056	-1.18798
O	2.05406	4.50508	-0.49721
O	-2.61107	-3.72968	-0.2768
O	4.12719	-2.49963	-1.20008
N	-1.97221	0.23238	1.17576
N	0.43545	1.96319	1.50633
N	0.10791	-1.90235	1.32226
N	2.47073	-0.11092	0.9889
C	-2.0622	-0.90293	2.15145
C	1.69625	1.86671	2.33103
C	-0.70549	-1.52672	2.53113
C	2.87222	1.19414	1.61241
C	-0.66781	1.93211	2.52703
C	2.35382	-1.07711	2.13865
C	-2.02494	1.51517	1.9571
C	1.46392	-2.29137	1.83634
C	-3.31616	0.23367	0.45457
C	0.45137	3.39315	0.98427
C	-0.4947	-3.20639	0.83018
C	3.69963	-0.55641	0.21939
C	-3.25728	1.18609	-0.76352
C	1.37719	3.4971	-0.2592
C	-1.64016	-2.96464	-0.18416
C	3.33422	-1.61359	-0.85501
H	-2.56554	-0.59325	3.10865
H	-2.68147	-1.72803	1.68817
H	2.05987	2.88553	2.65067
H	1.49661	1.3018	3.28545
H	3.70676	1.05891	2.35347
H	3.23518	1.886	0.79578
H	3.36126	-1.4781	2.44581
H	1.93573	-0.54801	3.03875
H	1.38818	-2.91053	2.77123
H	1.97976	-2.90619	1.04038
H	-0.91755	-2.41963	3.18337
H	-0.1129	-0.79837	3.15038
H	-2.39093	2.32682	1.26091
H	-2.75193	1.45427	2.81431
H	-0.41419	1.20231	3.34788
H	-0.79737	2.93988	3.01352
H	-4.15136	0.50924	1.14595
H	-3.49752	-0.79817	0.03723

Atom	X	Y	Z
H	-0.58801	3.66018	0.64996
H	0.76419	4.12864	1.76966
H	0.28966	-3.78134	0.26386
H	-0.85527	-3.84329	1.67863
H	4.11269	0.32551	-0.34399
H	4.50549	-0.94422	0.89403
Lu	0.18332	0.11636	-0.57983
O	-0.80491	-0.13632	-2.93235
H	-1.46856	-0.78859	-2.67364
H	-1.28929	0.69278	-3.00676

Cartesian coordinate of [Lu(3p-*C*-NETA)(H$_2$O)]$^-$ complex

Atom	X	Y	Z
O	-4.37405	-1.12419	-1.06605
O	-2.86592	4.00694	-2.002
O	-6.09542	-2.32693	-0.29842
O	-1.84808	2.11711	-1.36931
N	-3.57806	-1.02643	1.57993
N	-3.85176	1.61895	0.36482
N	-1.45976	0.80772	1.8903
C	-1.41052	-0.33638	2.8135
C	-2.66029	-1.28508	2.70814
C	-2.43809	1.78295	2.41147
C	-3.20616	2.52062	1.31997
C	-4.74007	-0.17199	1.92463
C	-5.04151	0.95049	0.90153
C	-4.07875	-2.28386	0.98246
C	-4.16386	2.36564	-0.86235
C	-0.17277	1.51121	1.72397
C	-4.95745	-1.91444	-0.24374
C	-2.84956	2.91342	-1.48739
H	-0.54087	-0.94361	2.59888
H	-1.31639	0.02776	3.84442
H	-3.21986	-1.27064	3.64743
H	-2.25225	-2.28194	2.57021
H	-3.12102	1.2626	3.06907
H	-1.92443	2.52666	3.03137
H	-2.50996	3.15191	0.77299
H	-3.95061	3.17609	1.79157
H	-5.63743	-0.79411	1.97277
H	-4.60549	0.24192	2.91845
H	-5.56888	0.51133	0.06081
H	-5.70601	1.68022	1.38403
H	-3.22486	-2.88001	0.65846
H	-4.68328	-2.85254	1.69154
H	-4.63218	1.68053	-1.5713
H	-4.83332	3.2093	-0.67755
H	-0.34398	2.31575	1.00565
H	0.11772	1.95891	2.68347

C	1.02098	0.67204	1.242
N	0.76733	0.01628	-0.05995
C	2.26459	1.58926	1.26234
C	1.15134	0.80918	-1.24221
C	1.29807	-1.36078	-0.0543
C	0.80421	0.06117	-2.55353
O	1.60117	0.10421	-3.46176
O	-0.32162	-0.55418	-2.5311
C	0.39598	-2.21218	0.86455
O	-0.83968	-2.22912	0.51473
O	0.86784	-2.73655	1.85482
C	3.59275	0.86735	0.99129
C	4.74229	1.88341	0.83484
C	8.39084	-0.1719	0.01673
C	7.50605	0.05343	-1.02472
C	6.33052	0.73315	-0.74678
C	6.04882	1.17898	0.5469
C	6.96324	0.92201	1.56812
C	8.14621	0.2439	1.31308
H	7.74314	-0.29679	-2.01618
H	5.62178	0.91853	-1.54224
H	6.74887	1.25804	2.57247
H	8.86842	0.03783	2.08616
N	9.64777	-0.88053	-0.26585
O	10.40063	-1.07186	0.6545
O	9.85292	-1.22523	-1.39975
H	2.12687	2.39537	0.53973
H	3.81755	0.18184	1.80972
H	4.5088	2.55698	0.01005
H	0.57206	1.73535	-1.24756
H	2.31922	-1.42394	0.31674
H	1.201	-0.12331	1.96468
H	2.32697	2.05095	2.24975
H	3.53913	0.2764	0.08038
H	4.83696	2.48052	1.74142
H	2.21617	1.03487	-1.29043
H	1.24295	-1.76044	-1.06437
Lu	-2.05367	-0.2959	-0.68055
O	-1.74014	-2.71203	-2.02649
H	-1.08695	-2.28973	-2.60859
H	-1.27445	-3.08467	-1.26572

Cartesian coordinate of [Lu(3p-*C*-DEPA)]$^{2-}$ complex

Atom	X	Y	Z
O	1.67348	2.6483	-1.05876
O	-3.30367	3.66673	-2.35801
O	-5.85636	-1.93903	-1.50189
O	0.14692	1.07245	-0.85248
O	-2.53286	1.65834	-1.85765
O	-3.89074	-0.93427	-1.41141

N	-1.25103	2.59306	0.84052
N	-1.10733	-0.26749	2.2826
N	-4.1837	1.71226	0.45231
N	-3.99223	-1.14328	1.40291
C	-2.42371	3.38182	1.17606
C	-2.1903	-0.86462	3.10956
C	-3.70046	2.60307	1.49057
C	-3.21448	-1.78644	2.44669
C	-0.80592	1.06403	2.84989
C	-4.9301	-0.16842	1.92488
C	-0.38491	2.22335	1.94659
C	-5.30676	0.92166	0.92905
C	-0.44375	3.23939	-0.19049
C	0.03139	-1.2207	2.32967
C	-4.51009	2.40001	-0.79034
C	-4.66128	-2.09315	0.51602
C	0.56046	2.25239	-0.77426
C	-3.33802	2.61323	-1.75899
C	-4.838	-1.6137	-0.93476
H	-2.22843	4.03336	2.03647
H	-2.62933	4.04448	0.34787
H	-1.74848	-1.41763	3.94223
H	-2.73667	-0.06017	3.57158
H	-3.8593	-2.13772	3.26623
H	-2.74211	-2.65827	2.03634
H	-5.85851	-0.65618	2.24354
H	-4.52538	0.28474	2.81763
H	-6.06735	1.55904	1.40208
H	-5.78604	0.46272	0.07962
H	-4.46633	3.35289	1.73905
H	-3.54705	2.02613	2.3904
H	0.58989	2.02172	1.54599
H	-0.24717	3.07603	2.62654
H	-1.68058	1.40144	3.38256
H	-0.02788	0.97424	3.61349
H	0.0982	4.10457	0.19784
H	-1.07683	3.57325	-0.99766
H	0.51507	-1.12584	3.30766
H	-5.21082	1.78689	-1.34163
H	-4.98957	3.36303	-0.6081
H	-4.06387	-2.98744	0.45271
H	-5.64404	-2.36698	0.90049
Lu	-1.76095	-0.27822	-0.89594
H	-0.40955	-2.20432	2.32616
C	1.19623	-1.2813	1.29626
H	1.78283	-2.10703	1.71712
C	2.13088	-0.06457	1.33639
H	1.81062	0.66768	0.62152
H	2.05314	0.392	2.32007
N	0.74027	-1.68923	-0.04348

C	1.56793	-1.38551	-1.20952
H	2.41456	-2.06508	-1.29952
H	1.93532	-0.37686	-1.16553
C	0.38189	-3.10458	-0.06377
H	1.0284	-3.69997	0.57869
H	0.50509	-3.48766	-1.06869
C	0.78034	-1.46646	-2.53633
O	1.42111	-1.73452	-3.52206
O	-0.46033	-1.23102	-2.47336
C	-1.07225	-3.36489	0.29481
O	-1.85622	-2.45033	-0.04373
O	-1.36066	-4.39824	0.8649
C	3.61188	-0.37739	1.09707
H	3.73751	-0.99648	0.21892
H	4.01827	-0.94682	1.93258
C	4.41356	0.92179	0.91155
H	4.34196	1.52502	1.8128
H	3.96038	1.50105	0.11581
C	5.86749	0.66865	0.59704
C	6.28225	0.47279	-0.71938
C	6.82309	0.60032	1.60831
C	7.6048	0.21827	-1.02067
H	5.55953	0.5235	-1.51317
C	8.15039	0.34775	1.32725
H	6.52307	0.75113	2.62999
C	8.52686	0.16026	0.01017
H	7.92088	0.07001	-2.03328
H	8.88375	0.29874	2.10638
N	9.92775	-0.09822	-0.29612
O	10.6984	-0.14668	0.61111
O	10.23359	-0.24644	-1.43517

B.2 Cartesian coordinates of Bi^{3+} complexes

Cartesian coordinate of [Bi(DOTA)(H$_2$O)]$^-$complex

Atom	X	Y	Z
O	-1.95557	1.48216	-1.37571
O	1.57145	1.80982	-1.42933
O	-1.84193	-1.83925	-0.73787
O	1.55152	-1.97195	-1.251
O	-4.14113	1.96405	-1.36698
O	2.53059	3.77595	-0.96917
O	-3.16521	-3.15769	0.48567
O	3.42563	-3.09277	-0.77942
N	-2.0572	0.59615	1.1513
N	0.55363	2.07843	1.20971
N	-0.08172	-1.76752	1.44825
N	2.40216	-0.18642	0.76689

Atom	X	Y	Z
C	-2.07277	-0.4052	2.23105
C	1.86331	1.99753	1.88173
C	-0.69796	-1.01892	2.55268
C	2.90685	1.14248	1.1446
C	-0.51445	2.29791	2.1959
C	2.29048	-1.05071	1.95228
C	-1.90101	1.97334	1.64673
C	1.27964	-2.19648	1.81646
C	-3.30529	0.56202	0.35988
C	0.5516	3.17471	0.21354
C	-0.87112	-2.96218	1.10184
C	3.31754	-0.77379	-0.22914
C	-3.15471	1.42763	-0.91826
C	1.66386	2.93792	-0.83503
C	-2.09771	-2.6423	0.22148
C	2.74867	-2.08763	-0.80451
H	-2.4552	0.04243	3.1567
H	-2.76088	-1.20167	1.95726
H	2.28631	2.99978	2.01119
H	1.70441	1.58395	2.87645
H	3.77672	1.0419	1.80831
H	3.23661	1.64981	0.24514
H	3.26463	-1.50278	2.1744
H	2.02478	-0.43332	2.80682
H	1.25553	-2.7293	2.77724
H	1.62545	-2.89398	1.06121
H	-0.82638	-1.68208	3.41971
H	-0.00952	-0.22868	2.83435
H	-2.12467	2.64649	0.82319
H	-2.63665	2.16707	2.43808
H	-0.32274	1.68209	3.07151
H	-0.51585	3.34225	2.53305
H	-4.15297	0.94369	0.93457
H	-3.5011	-0.45861	0.03782
H	-0.40386	3.17972	-0.31183
H	0.72825	4.13649	0.7009
H	-0.23901	-3.60904	0.49588
H	-1.20006	-3.49695	1.9968
H	3.40401	-0.0635	-1.05108
H	4.29951	-0.97466	0.20628
Bi	-0.04468	-0.00608	-0.78182
O	-0.39929	-1.57068	-2.98631
H	0.35606	-2.12535	-2.73026
H	-1.20499	-1.97397	-2.63167

Cartesian coordinate of [Bi(3p-*C*-NETA)(H₂O)]⁻ complex

Atom	**X**	**Y**	**Z**

O	-4.11044	-0.16535	-1.48007
O	-2.78674	4.19315	-0.1054
O	-5.8997	-1.47397	-1.66689
O	-1.9334	2.15701	-0.37098
N	-3.63355	-1.67307	0.87875
N	-3.92243	1.142	1.06629
N	-1.48389	-0.12099	2.04375
C	-1.38941	-1.57837	2.21566
C	-2.61726	-2.41132	1.6451
C	-2.46414	0.45142	2.97092
C	-3.2976	1.55875	2.32297
C	-4.7762	-1.15695	1.63178
C	-5.1091	0.30702	1.25646
C	-4.08744	-2.31814	-0.3635
C	-4.22475	2.3197	0.24832
C	-0.21717	0.62824	2.1597
C	-4.78127	-1.25825	-1.26942
C	-2.89387	2.99577	-0.11346
H	-0.50629	-1.94598	1.70368
H	-1.27176	-1.81398	3.27945
H	-3.09368	-2.94884	2.46824
H	-2.16699	-3.13987	0.97553
H	-3.10274	-0.34456	3.33365
H	-1.95866	0.8705	3.84918
H	-2.64251	2.40277	2.11462
H	-4.05762	1.90252	3.03616
H	-5.66794	-1.75377	1.41519
H	-4.58736	-1.25171	2.69638
H	-5.66295	0.30724	0.32282
H	-5.75858	0.73047	2.03341
H	-3.22989	-2.71506	-0.90565
H	-4.81214	-3.11087	-0.17588
H	-4.70129	1.98045	-0.67027
H	-4.85003	3.04984	0.76655
H	-0.45179	1.67194	1.94111
H	0.14125	0.56612	3.19558
C	0.95873	0.1843	1.26379
N	0.63021	0.17611	-0.17861
C	2.18598	1.04203	1.64107
C	0.84886	1.43188	-0.90424
C	1.24836	-0.9676	-0.89619
C	0.16905	1.41485	-2.30119
O	0.66757	2.0679	-3.17977
O	-0.88664	0.66675	-2.41206
C	0.75815	-2.30003	-0.27152
O	-0.36405	-2.71053	-0.67418
O	1.44923	-2.78815	0.62182
C	3.50445	0.5242	1.04546
C	4.71062	1.24536	1.68242
C	8.34453	-0.13378	-0.08063

C	7.73652	0.98966	-0.61281
C	6.56188	1.43589	-0.02579
C	6.01025	0.77294	1.07131
C	6.64858	-0.36567	1.56645
C	7.82369	-0.82996	0.9967
H	8.18016	1.48933	-1.45854
H	6.06646	2.30966	-0.42435
H	6.21826	-0.89377	2.40532
H	8.33345	-1.70495	1.36573
N	9.59977	-0.60636	-0.68225
O	10.11818	-1.58095	-0.202
O	10.03973	0.0111	-1.61695
H	2.02799	2.08274	1.35213
H	3.58643	-0.5507	1.21288
H	4.60928	2.32049	1.53545
H	0.38738	2.25496	-0.36112
H	2.33529	-0.9291	-0.8436
H	1.21412	-0.8389	1.5262
H	2.2786	1.01827	2.72949
H	3.53475	0.6921	-0.02947
H	4.72464	1.05215	2.75489
H	1.9038	1.64144	-1.08535
H	0.92533	-0.91469	-1.93225
Bi	-2.03367	-0.05949	-0.58613
O	-1.88239	-1.80188	-2.58025
H	-1.50975	-1.17889	-3.21478
H	-1.17124	-2.28599	-2.10168

Cartesian coordinate of [Bi(3p-*C*-DEPA)]²⁻ complex

Atom	X	Y	Z
O	1.79868	3.24656	0.30833
O	-3.08623	4.03309	-1.9986
O	-5.20953	-2.22282	-2.4701
O	0.64525	1.44678	-0.31077
O	-2.04833	2.05968	-1.89276
O	-3.37625	-1.02394	-2.03287
N	-1.47895	2.38458	1.04895
N	-1.40406	-0.49184	2.32263
N	-4.09683	1.25769	-0.10979
N	-3.79033	-1.59093	0.66997
C	-2.80727	2.98984	1.19617
C	-2.59166	-1.2446	2.81978
C	-3.97247	2.00002	1.14371
C	-3.24593	-2.24717	1.86013
C	-1.36074	0.79827	3.05378
C	-4.98446	-0.80793	0.98594
C	-0.83972	2.04037	2.32269
C	-5.22656	0.32917	-0.00734
C	-0.58519	3.33913	0.35995

C	-0.22514	-1.36153	2.59945
C	-4.32461	2.1362	-1.26381
C	-4.12273	-2.56641	-0.38114
C	0.75433	2.64445	0.07661
C	-3.0407	2.82924	-1.7696
C	-4.26708	-1.88949	-1.76603
H	-2.87407	3.53128	2.15103
H	-2.93926	3.72321	0.4036
H	-2.32032	-1.77967	3.73935
H	-3.34954	-0.52034	3.10159
H	-4.04843	-2.74175	2.4317
H	-2.54163	-3.00959	1.54383
H	-5.87309	-1.45358	0.97472
H	-4.91041	-0.40419	1.99266
H	-6.13251	0.87121	0.30864
H	-5.41827	-0.08729	-0.99018
H	-4.89608	2.57155	1.33407
H	-3.85636	1.27962	1.94836
H	0.21982	1.92998	2.14001
H	-0.94837	2.87705	3.03136
H	-2.36807	1.03384	3.38754
H	-0.75663	0.68758	3.96364
H	-0.39739	4.21981	0.98291
H	-1.02902	3.62756	-0.58984
H	-0.01776	-1.31768	3.67937
H	-4.65388	1.50345	-2.08642
H	-5.08079	2.89886	-1.04628
H	-3.30028	-3.26983	-0.45942
H	-5.05935	-3.08609	-0.1555
Bi	-1.42306	-0.10858	-0.68997
H	-0.54174	-2.38011	2.38647
C	1.14856	-1.18014	1.89434
H	1.73477	-1.99164	2.35541
C	1.88868	0.12504	2.2389
H	1.57667	0.88146	1.52809
H	1.60203	0.44407	3.24286
N	1.06308	-1.42822	0.44155
C	2.1467	-0.89378	-0.38607
H	3.04337	-1.52112	-0.34632
H	2.37729	0.12269	-0.09839
C	0.9598	-2.86493	0.15874
H	1.65242	-3.44796	0.77357
H	1.18943	-3.01343	-0.89467
C	1.75542	-0.75984	-1.88051
O	2.69765	-0.59105	-2.64375
O	0.52114	-0.82054	-2.15396
C	-0.46772	-3.37914	0.33984
O	-1.33308	-2.63699	-0.20383
O	-0.68234	-4.40471	0.98147
C	3.42966	-0.01939	2.15938

Atom	X	Y	Z
H	3.67928	-0.89085	1.55962
H	3.84886	-0.19519	3.15187
C	4.10459	1.23054	1.52478
H	4.32185	1.96724	2.29801
H	3.43167	1.71343	0.81539
C	5.38229	0.83347	0.82072
C	5.35069	0.43729	-0.52256
C	6.59783	0.80183	1.50957
C	6.50846	0.01357	-1.15938
H	4.4238	0.44268	-1.08424
C	7.76604	0.38814	0.88938
H	6.62477	1.11039	2.54552
C	7.69357	0.00127	-0.43897
H	6.49106	-0.30058	-2.1906
H	8.71296	0.36124	1.4035
N	8.92789	-0.43442	-1.10097
O	9.94544	-0.4525	-0.4481
O	8.87033	-0.75138	-2.26034

B.3 Cartesian coordinates of Ac^{3+} complexes

Cartesian coordinate of [Ac(DOTA)(H$_2$O)]$^-$complex

Atom	X	Y	Z
O	-1.68064	1.51603	-1.19104
O	1.36684	1.67614	-1.3471
O	-1.7094	-1.49417	-1.00593
O	1.20431	-1.78731	-1.35848
O	-3.86496	1.90424	-1.45026
O	2.28492	3.69355	-1.06288
O	-3.05131	-3.06954	-0.1773
O	3.05819	-3.03208	-1.37481
N	-1.99345	0.41115	1.18691
N	0.56713	1.89211	1.28443
N	-0.05136	-1.87944	1.21162
N	2.3573	-0.26277	0.60049
C	-2.08176	-0.71396	2.13213
C	1.9205	1.82971	1.86998
C	-0.73411	-1.39349	2.41892
C	2.91805	1.02609	1.02381
C	-0.43482	2.00299	2.35112
C	2.29634	-1.18577	1.743
C	-1.84284	1.71917	1.84357
C	1.30768	-2.34006	1.55279
C	-3.20137	0.50354	0.34294
C	0.48532	3.04672	0.35938
C	-0.79088	-2.98972	0.57647
C	3.16943	-0.81601	-0.49893
C	-2.92338	1.39931	-0.88338

C	1.47864	2.82472	-0.80282
C	-1.9821	-2.49802	-0.26773
C	2.44149	-2.0097	-1.1504
H	-2.5041	-0.38297	3.0881
H	-2.76054	-1.45701	1.71985
H	2.32083	2.8399	2.00108
H	1.84292	1.38181	2.85893
H	3.82331	0.87008	1.62523
H	3.19694	1.5874	0.1397
H	3.28753	-1.61517	1.93099
H	2.0162	-0.61739	2.62698
H	1.28356	-2.92581	2.48028
H	1.66143	-2.99231	0.7625
H	-0.92043	-2.23183	3.10266
H	-0.06744	-0.69692	2.9202
H	-2.11502	2.48245	1.11931
H	-2.54346	1.80003	2.68359
H	-0.18633	1.29557	3.13922
H	-0.41796	3.0068	2.79379
H	-4.0429	0.9287	0.89614
H	-3.46926	-0.4767	-0.03987
H	-0.5085	3.08837	-0.08052
H	0.73502	3.9757	0.87638
H	-0.11603	-3.46238	-0.13408
H	-1.14315	-3.71003	1.31834
H	3.2566	-0.03974	-1.25782
H	4.15471	-1.13385	-0.15058
Ac	0.00263	0.00654	-0.57675
O	-0.3407	-0.28744	-2.95167
H	0.41409	-0.36032	-3.54038
H	-1.23183	-0.33131	-3.30603

Cartesian coordinate of [Ac(3p-*C*-NETA)(H₂O)]⁻ complex

Atom	X	Y	Z
O	-4.411	-1.37	2.968
O	-3.805	-4.848	-1.625
O	-6.149	-0.442	4.082
O	-2.756	-3.517	-0.124
N	-4.004	0.745	1.453
N	-4.4	-1.493	-0.401
N	-2.137	0.395	-0.592
C	-2.252	1.813	-0.067
C	-3.28	2.002	1.078
C	-3.16	0.316	-1.702
C	-3.995	-0.967	-1.746
C	-5.219	0.691	0.564
C	-5.587	-0.707	0.052
C	-4.588	0.983	2.836
C	-4.941	-2.874	-0.725
C	-0.825	0.34	-1.329

C	-5.136	-0.37	3.373
C	-3.757	-3.868	-0.871
H	-1.254	2.104	0.371
H	-2.482	2.533	-0.898
H	-3.987	2.829	0.801
H	-2.687	2.334	1.983
H	-3.864	1.191	-1.647
H	-2.67	0.398	-	2.716
H	-3.387	-1.774	-2.253
H	-4.891	-0.759	-2.395
H	-6.14	1.062	1.104
H	-5.096	1.376	-0.319
H	-6.073	-1.271	0.903
H	-6.347	-0.591	-0.769
H	-3.766	1.317	3.528
H	-5.382	1.773	2.832
H	-5.574	-3.229	0.132
H	-5.571	-2.867	-1.651
H	-0.83	-0.58	-1.98
H	-0.717	1.242	-1.996
C	0.423	0.291	-0.417
N	0.301	-0.707	0.704
C	1.618	0.184	-1.381
C	1.177	-1.895	0.398
C	1.015	-0.026	1.865
C	0.959	-3.006	1.46
O	1.857	-3.783	1.806
O	-0.257	-2.99	1.919
C	0.068	0.978	2.558
O	-1.152	0.53	2.595
O	0.44	2.08	2.986
C	2.92	0.702	-0.806
C	3.981	0.752	-1.893
C	7.903	1.622	-0.417
C	7.264	0.432	-0.032
C	5.983	0.166	-0.505
C	5.33	1.071	-1.353
C	5.974	2.261	-1.715
C	7.256	2.546	-1.254
H	7.774	-0.284	0.636
H	5.478	-0.767	-0.207
H	5.464	2.984	-2.37
H	7.759	3.483	-1.543
N	9.279	1.907	0.06
O	9.812	2.934	-0.271
O	9.836	1.103	0.76
H	1.752	-0.865	-1.75
H	2.772	1.726	-0.374
H	4.029	-0.247	-2.409
H	0.876	-2.326	-0.594

Atom	X	Y	Z
H	1.958	0.485	1.542
H	0.502	1.319	0.061
H	1.378	0.807	-2.287
H	3.28	0.039	0.024
H	3.686	1.511	-2.667
H	2.264	-1.63	0.37
H	1.289	-0.814	2.62
Ac	-2.316	-1.484	1.43
O	-1.436	-1.961	3.794
H	-1.026	-2.828	3.714
H	-0.714	-1.327	3.725

Cartesian coordinate of [Ac(3p-*C*-DEPA)]²⁻ complex

Atom	X	Y	Z
O	1.91169	2.96331	-0.7639
O	-3.52888	4.13434	-1.88834
O	-6.14251	-1.93069	-1.24094
O	0.4563	1.31509	-0.99115
O	-2.68296	2.08946	-1.81913
O	-4.175	-0.92992	-1.41062
N	-1.08923	2.47916	0.94305
N	-0.95274	-0.44633	2.27234
N	-4.09991	1.69751	0.6138
N	-3.88652	-1.24455	1.38838
C	-2.25039	3.24373	1.39256
C	-2.03857	-1.06193	3.08253
C	-3.51367	2.44992	1.71284
C	-3.07887	-1.93975	2.38449
C	-0.61252	0.85559	2.88697
C	-4.80179	-0.2878	1.99571
C	-0.19672	2.03869	2.01116
C	-5.20444	0.87286	1.09274
C	-0.29956	3.29293	0.00571
C	0.17142	-1.42232	2.25569
C	-4.56077	2.5641	-0.47186
C	-4.62442	-2.19071	0.54239
C	0.80621	2.46753	-0.65539
C	-3.48684	2.99116	-1.48647
C	-5.04301	-1.63325	-0.82985
H	-2.00278	3.82391	2.28792
H	-2.48882	3.97075	0.63148
H	-1.59808	-1.6624	3.88116
H	-2.5648	-0.27042	3.58876
H	-3.71062	-2.33859	3.19006
H	-2.61386	-2.78514	1.91316
H	-5.72394	-0.78886	2.30417
H	-4.3716	0.09849	2.90719
H	-5.92938	1.48314	1.64811
H	-5.72906	0.48512	0.23596
H	-4.24255	3.17068	2.10724

H	-3.30374	1.76628	2.51956
H	0.75628	1.83079	1.56825
H	-0.01683	2.86322	2.7127
H	-1.46069	1.18256	3.46702
H	0.19068	0.72266	3.61547
H	0.14737	4.15028	0.51074
H	-0.94852	3.65598	-0.77721
H	0.66594	-1.38424	3.23139
H	-5.28721	2.0106	-1.05301
H	-5.05739	3.455	-0.08587
H	-3.97932	-3.02838	0.33342
H	-5.51456	-2.55613	1.05401
Ac	-1.78158	-0.15115	-0.87891
H	-0.28431	-2.39729	2.20492
C	1.32082	-1.43388	1.20457
H	1.91767	-2.27551	1.57409
C	2.24413	-0.20869	1.28618
H	1.91366	0.54432	0.59523
H	2.16171	0.21317	2.28418
N	0.8441	-1.77421	-0.14939
C	1.69965	-1.4282	-1.28788
H	2.55988	-2.09113	-1.36499
H	2.04552	-0.41317	-1.20481
C	0.50303	-3.19744	-0.23628
H	1.20046	-3.80908	0.33346
H	0.5824	-3.51019	-1.26913
C	0.95994	-1.47726	-2.64321
O	1.62849	-1.76668	-3.60744
O	-0.26488	-1.18097	-2.61969
C	-0.92581	-3.53207	0.17714
O	-1.77893	-2.69632	-0.19352
O	-1.12471	-4.54961	0.81421
C	3.73104	-0.48648	1.04185
H	3.87593	-1.04256	0.12579
H	4.13489	-1.10578	1.84231
C	4.51593	0.83367	0.95706
H	4.43127	1.36763	1.89988
H	4.06127	1.46724	0.20473
C	5.97513	0.62188	0.63608
C	6.40513	0.55085	-0.68783
C	6.92093	0.46941	1.64749
C	7.7331	0.33566	-0.99649
H	5.69034	0.66872	-1.48159
C	8.25323	0.25453	1.35933
H	6.60915	0.52419	2.67531
C	8.64487	0.19121	0.03478
H	8.06094	0.28325	-2.01483
H	8.979	0.14074	2.13878
N	10.05122	-0.02657	-0.27835
O	10.81281	-0.1518	0.62912

O   10.37014   -0.06704   -1.4227

Appendix

Research achievements

1. **D. Ramdhani**, H. Watabe, A. Hardianto, R.S Janitra. "Complexation of 3p-*C*-NETA with Radiometal Ions: A Density Functional Theory Study for Targeted Radioimmunotherapy". *Heliyon* (Submitted, December 2023)

2. **D. Ramdhani**, N. Listiani, M.E Sriyani, E. Maria, R. Mustarichie, H. Watabe, S. Agung F.K, R.S Janitra Estrogen receptor targeting with genistein radiolabeled Technetium-99^m as radiotracer of breast cancer: Its optimization, characterization, and predicting formation constants by DFT calculation. *Heliyon*, Vol. 9, (2023) e13169. https://doi.org/10.1016/j.heliyon.2023.e13169.

3. Stephen Ahenkorah, **Danni Ramdhani**, Christophe Deroose, Thomas Cardinaels, Guy Bormans, Frederik Cleeren, Maarten Ooms. Evaluation of 3p-*C*-DEPA as potential ^{225}Ac-chelator. *Nuclear Medicine and Biology*, 114–115/S (2022) S32–S75. DOI: 10.1016/S0969-8051(22)02189-8

4. **Danni Ramdhani**, Sri Agung F.K, Dede Sediana, A.P. Hilarius Bima, Ika Khumairoh. Comparative study of cefixime and tetracycline as an evaluation policy driven by the antibiotic resistance crisis in Indonesia. *Scientific Reports*, (2021) 11:1846.
https://doi.org/10.1038/s41598-021-98129-y

5. **D. Ramdhani**, E.M Widyasari, M.E Sriyani, Q.P Arnanda, H. Watabe. Iodine-131 labeled genistein as a potential radiotracer for breast cancer. *Heliyon.* Vol. 6, (2020). Issue 9, E04780.
https://doi.org/10.1016/j.heliyon.2020.e04780